



Conversion of glycerol over 10%Ni/γ-Al₂O₃ catalyst

B.C. Miranda ^{a,b}, R.J. Chimentão ^{a,*}, J.B.O. Santos ^c, F. Gispert-Guirado ^a, J. Llorca ^d, F. Medina ^a, F. López Bonillo ^a, J.E. Sueiras ^a

^a Universitat Rovira I Virgili, Tarragona 43007, Spain

^b Universidad de Costa Rica, San José 2060, Costa Rica

^c Universidade Federal de São Carlos, São Carlos, Brazil

^d Universitat Politècnica de Catalunya, Barcelona, Spain



ARTICLE INFO

Article history:

Received 15 July 2013

Received in revised form

17 September 2013

Accepted 19 September 2013

Available online 27 September 2013

Keywords:

Hydrogenolysis

Dehydration

Glycerol

Nickel

Catalyst

ABSTRACT

The conversion of glycerol in gas phase and atmospheric pressure has been investigated over 10 wt.% Ni/γ-Al₂O₃ catalyst. The catalysts were prepared with nickel nitrate and pre-treated with hydrogen in the range of 623–1073 K. The resultant catalysts were characterized by N₂-physisorption, H₂-chemisorption, X-ray diffraction (XRD), TGA-MS, TEM, RAMAN, NH₃-TPD, XPS, TPO-MS and XANES. The stability and the catalytic behavior of the catalysts were affected by the reduction pre-treatment. Glycerol reaction pathways were proposed based on dehydration, dehydrogenation and hydrogenolysis steps. The main products identified were: hydroxyacetone, pyruvaldehyde, pyruvic acid, lactic acid, lactide, acetaldehyde and methane. The number of exposed Ni atoms and the degree of reduction of the NiO species affected the hydrogenolysis reaction of glycerol to CH₄ affecting the catalytic stability. The catalyst was deactivated by coke formation, by transformation of Ni phase to nickel carbide (Ni₃C), as well as by oxidation of the Ni phase during the reaction. In addition, Raman analysis revealed two types of carbonaceous deposits over the used samples: on the Ni species and on the support. The regeneration treatment by oxidation–reduction reactivated the catalyst successfully.

© 2013 Elsevier B.V. All rights reserved.

1. Introduction

Glycerol is an important molecular building block in the production of many high-value chemicals. During the production of biodiesel by transesterification of vegetable oils, around 10% of glycerol is generated as byproduct, leading to large surpluses of this material [1]. Therefore, many efforts have been reported on the conversion of glycerol into value-added products, such as catalytic oxidation of glycerol to glyceric acid [2] and dihydroxyacetone [3], dehydration of glycerol to acrolein, and hydrogenolysis of glycerol to polyols and alcohols [4].

Hydrogenolysis and dehydration of glycerol provides a route for the production of these commodity chemicals from renewable glycerol instead of fossil oil [5]. Acid catalyzed dehydration followed by metal-catalyzed hydrogenation and/or hydrogenolysis reactions result in a net removal of oxygen atoms in the glycerol molecule. The conversion of glycerol has been investigated both in liquid and gas phases. The conversion of glycerol in liquid phase is usually carried out at temperatures ranging from 393 K to 533 K and pressures of 1–50 MPa using noble metals [6–12]. However, one drawback of the liquid phase reaction is the use of high

pressure equipment which can increase the selectivity to degradation products [13].

Several routes have been suggested for glycerol hydrogenolysis [14–16]. Two typical reaction routes leading to the formation of hydroxyacetone involving different catalytic functions have been proposed. The first route, proposed by Dasari et al. [14], involves direct dehydration of glycerol on solid acid catalysts. In the second route, proposed by Montassier et al. [17], glycerol dehydrogenates to form glyceraldehyde or dihydroxyacetone intermediates on metal surfaces followed by their dehydration and subsequent hydrogenation into hydroxyacetone. Besides dehydration and hydrogenation reactions, direct hydrogenolysis of glycerol to form respectively 1,2-propanediol (1,2-PDO), 1,3-propanediol (1,3-PDO) and ethylene glycol (EG) and progressive degradation toward methane (CH₄) may occur simultaneously. The diols can undergo further hydrogenolysis to form primary alcohols such as 1-propanol (1-PO), ethanol and methanol, as well as secondary alcohols like 2-propanol (2-PO). 1,2-PDO and EG are two of the most interesting chemicals produced through glycerol catalytic transformation, which are important chemicals used in antifreeze, paints, functional fluids, humectants, and polyester and which are nowadays obtained by the petrochemical route.

Different catalytic metals such as Pd [18], Pt [19,20], Cu [21], Cu–Ru [22], Ni [14], Ni–Ce [23], Pd–Cu [24], Ru–Re [25], Raney Ni [26] have been tested in the conversion of glycerol. The metal phase

* Corresponding author. Tel.: +34 977 55 8547.

E-mail address: ricardojose.chimenton@urv.cat (R.J. Chimentão).

has both hydrogenating and dehydrogenating functions, and the acid sites of the support has both hydration and dehydration functions, both phases forming together a bifunctional catalyst [27,28]. The Ni/ γ -Al₂O₃ ability for hydrogenation–dehydrogenation along with its acid properties constitute a determinant bifunctional property which is needed to obtain important secondary chemicals like hydroxyacetone, pyruvaldehyde and acetaldehyde [29]. The main disadvantage of supported Ni catalysts compared with noble metal catalysts is their lower stability due to carbon deposition. Nickel promotes C–C bond cleavage, providing a source of carbon. The presence of defects in the crystalline structure or low coordination number surface sites, which can be numerous on small particles, may lead to coke formation [30]. How to improve the stability of Ni-based catalysts by controlling the number of exposed atoms of the metal remains a matter of debate [13]. Previous studies indicated that Ni supported on alumina cannot be completely reduced to metallic state because of strong metal–support interaction [31,32]. The surface area of the catalyst, the degree of reduction and the number of exposed atoms of the metal on the support can strongly affect catalytic performance [32]. In addition, the effect of metal sintering on the catalytic behavior could be different depending on the catalytic reactions involved [33,34].

This work is focused on the catalytic conversion of glycerol in gas phase over 10%Ni/ γ -Al₂O₃ catalyst at atmospheric pressure in the presence of hydrogen and under argon flow in a fixed bed reactor. Different reduction pre-treatment of the Ni samples was used to evaluate its effect on the catalytic performance. The structure of catalysts was characterized using several techniques such as temperature-programmed desorption of ammonia (TPD-NH₃), thermogravimetric analysis (TGA), temperature-programmed reduction (TPR), X-ray diffraction (XRD), N₂-physisorption, H₂-chemisorption, transmission electron microscopy (TEM) and X-ray absorption near edge structure (XANES). The process of carbon deposition on used samples was characterized by temperature-programmed oxidation (TPO) coupled to a mass spectrometer (MS), Raman analysis, X-ray photoelectron spectroscopy (XPS) and high-resolution transmission electron microscopy (HRTEM).

2. Experimental

2.1. Catalyst preparation

Commercial γ -Al₂O₃ was purchased from Degussa and was calcined at 463 K for 4 h before use. The samples containing 10 wt.% of Ni were prepared by incipient wetness impregnation of γ -Al₂O₃ with a 4.8 M Ni(NO₃)₂·6H₂O (Aldrich, 99.999%) aqueous solution. After impregnation, the sample was dried at 373 K for 12 h and then reduced at different temperatures ($T_{\text{red}} = 623, 723, 823, 923, 993$ and 1073 K) in a flow of 20 mL/min with pure H₂ for 4 h. Each resultant material was labeled as NiT_{red} (for instance Ni623).

2.2. Catalyst characterization

2.2.1. Thermogravimetric analysis

The decomposition temperature of Ni(NO₃)₂·6H₂O precursor was investigated by TGA-MS over dried sample after impregnation of the Ni precursor aqueous solution. TGA were recorded in a Labsys/Setaran TG thermo balance apparatus from room temperature (RT) to 1173 K, at a heating rate of 10 K/min under a flow of 5%H₂/Ar. The off-gas was simultaneously analyzed with a Pfeiffer Vacuum QME 220 mass spectrometer (MS).

2.2.2. Temperature programmed reduction (TPR)

TPR experiments were performed in a ThermoFinnigan (TPORD 110) apparatus equipped with a thermal conductivity detector

(TCD). The samples were then purged with argon flow before the TPR. The analysis was carried out using a 5%H₂/Ar gas flowing at 20 mL/min by heating from RT to 1173 K with a heating rate of 10 K/min.

2.2.3. N₂-adsorption–desorption

The specific surface areas, cumulative pore volumes and average pore diameters of the samples were measured by the BET method using N₂ adsorption/desorption at 77 K in a Quantachrome Autosorb-1. Before measurement, each sample was degassed under vacuum at 393 K for 10 h. The BET specific surface area was calculated from the range $P/P_0 = 0.05$ –0.35 in the adsorption branch while the pore size distribution was calculated from the desorption branch.

2.2.4. X-ray diffraction

The XRD analysis of the materials was recorded using a Siemens D5000 diffractometer (Bragg–Bentano for focusing geometry and vertical θ – θ goniometer) with an angular 2 θ -diffraction range between 5° and 70°. The samples were dispersed on a Si(5 1 0) sample holder. Spectra were collected with an angular step of 0.03° at 5 s per step of sample rotation. Cu K α radiation ($\lambda = 1.54056$ Å) was obtained from a copper X-ray tube operated at 40 kV and 30 mA.

2.2.5. In situ X-ray diffraction

An *in situ* X-ray diffraction study was carried out at the beam line BM25A of the European Synchrotron Radiation Facility (ESRF, Grenoble, France). Samples in pellet shape (1.0 cm diameter and 0.25 cm thickness) were placed in a cell reactor (SPECAC Brilliant Spectroscopy) to be analyzed in transmission mode (2 mm × 2 mm of beam size). The diffracted X-rays were recorded on an x-axis motorized CCD detector (charge-coupled device) at 34 cm from the sample. The X-ray wavelength used was 0.6199 Å (20 keV) and the Bragg angle was scanned continuously in the range 2 θ = 2.2°–22°. The exposition time for the CCD detector was of 300 s. Approximately 100 mg of the dried sample with Ni(NO₃)₂·6H₂O precursor impregnated over γ -Al₂O₃ was placed in a metallic sample holder. The CCD images (*ca.* 68 scans) were acquired *in situ* while the sample was heated in a 50 mL/min H₂ stream (5%H₂/He) from 310 K to 1000 K at a rate of 2.5 K/min. Each CCD image was converted into conventional X-ray diffractograms by azimuthal integration (X-ray Oriented Programs, XOP 2.3 Software). Prior to each analysis, the CCD was calibrated by analyzing α -Al₂O₃ (SRM 676) prepared in the same conditions.

2.2.6. X-ray absorption near edge structure

XANES spectra at the Ni K-edge (8333 eV) for impregnated Ni sample were measured at the DXAS beamline of the Brazilian Synchrotron Light Laboratory (LNLS, Campinas, Brazil). The Ni impregnated sample was first crushed and sieved to particle sizes smaller than 20 μ m. A self-supported pellet (60.0 mg of catalyst diluted in 60.0 mg of boron nitride) was prepared and placed inside of a tubular quartz reactor (20 mm ID and 440 mm X-ray path length), equipped with kapton™ refrigerated windows. Then, temperature-resolved XANES spectra were acquired during *in situ* reduction of the sample using 5%H₂ in He, flowing at 100 mL/min, with heating at a rate of 10 K/min from RT to 973 K. Ni foil and NiO were used as standards samples to measure the valence state of metallic Ni and oxidized Ni.

2.2.7. Transmission electron microscopy

TEM study was carried out in a JEOL JEM-2100 instrument operating at an accelerating voltage of 100 kV. The samples were prepared by dispersing the as-prepared catalysts in alcohol and then dropping the aqueous suspension on a standard 3 mm holey carbon-coated copper grid and letting the water evaporate at RT.

High-resolution transmission electron microscopy (HRTEM) for the spent material Ni923 sample was carried out with a JEOL 2010F instrument equipped with a field emission source. The point-to-point resolution was 0.19 nm and the resolution between lines was 0.14 nm.

2.2.8. Temperature programmed desorption of NH_3

The total acidity measurements of the fresh catalysts were determined by TPD of NH_3 on a Thermo Finnigan TPDRO 1100 equipped with a TCD detector. Each sample (0.1 g) was pre-treated with Ar at 353 K during 1 h in a tubular down-flow quartz reactor and then cooled to RT. The sample was then treated with NH_3 flow (5% NH_3 in He) at RT for 1 h. The NH_3 desorption was measured by heating the sample from RT to 1073 K at a rate of 5 K/min in He flow. The total number of acid sites was calculated by using pulses of a known amount of NH_3 .

2.2.9. Temperature programmed oxidation (TPO)

The amounts of coke deposited on the spent catalysts were determined by TPO. These tests were carried out with a Sensys Evo apparatus. TPO profiles were obtained from approximately 20 mg of sample, placed in a quartz reactor (ID = 0.5 cm, length = 10 cm) and heated from 303 K to 1023 K at a rate of 10 K/min in air flow. The CO_2 produced was quantified on-line using a Pfeiffer Vacuum QME 220 mass spectrometer. In addition, the effect of time on stream on the catalytic conversion of glycerol on coke formation was investigated in order to get insights into the deactivation sources. A representative sample Ni723 was analyzed at different reaction times (1, 2 and 3 h) by TPO.

2.2.10. X-ray photoelectron spectroscopy

The XPS spectra were acquired in a VG Escalab 200R electron spectrometer equipped with a hemispherical electron analyzer, operating in a constant pass energy mode, and a non-monochromatic Mg-K α ($h\nu = 1253.6 \text{ eV}$, $1 \text{ eV} = 1.603 \times 10^{-19} \text{ J}$). X-ray source was operated at 10 mA and 1.2 kV. The angle of the incident photon beam was 45° with respect to the normal of the sample. The background pressure in the analysis chamber was kept below $7 \times 10^{-9} \text{ mbar}$ during data acquisition. The binding energy (BE C1s = 284.9 eV) of adventitious C1 was used as reference. A Shirley background subtraction was applied and Gaussian–Lorentzian product functions were used to approximate the line shapes of the fitting components.

2.2.11. Raman spectroscopy

Raman spectra of the spent 10%Ni/ γ -Al₂O₃ catalysts were obtained by using a T64000 Jobin Iyon spectrometer. Approximately, 10 mg of each sample was excited using an Ar laser operating at 514.5 nm and a power of 2 mW.

2.2.12. H_2 -chemisorption

H_2 -chemisorption was performed to determine the total area of the exposed metallic Ni atoms [35]. The analysis was performed using a conventional static method in a Micromeritics 2010 instrument. The samples were heated in flowing He at 400 K for 1 h; then the temperature was increased to the correspondent reduction temperature. At this temperature, the He flow was replaced by H_2 flow, and the samples were reduced for 2 h and subsequently out-gassed for 30 min. Finally, the samples were cooled to RT and evacuated at RT for 30 min. The hydrogen adsorption isotherm was recorded at RT. After evacuation at RT for 10 min, a second H_2 isotherm was obtained. The chemisorbed H_2 uptake was obtained by extrapolating to zero pressure the linear portion

of the isotherm. The number of exposed Ni atoms was calculated assuming spherical particles, the stoichiometry factor of 1 atomic chemisorbed hydrogen per surface Ni atom, a Ni surface area of 0.065 nm² per Ni atom and a Ni density of 8.9 g/cm³ [35].

2.3. Conversion of glycerol

The catalytic conversion of glycerol was carried out in gas phase in a quartz fixed bed down flow reactor at 573 K for 6 h. Gas flow rates were controlled by unit mass flow controllers. The feed gas composition during reaction was 5% H_2 in Ar. An aqueous solution of glycerol (3%, v/v) was pumped by a syringe pump with flow of 3.5 mL/h and injected into the reactive gas. Previous to entrance to the reactor the reactive mixture was preheated at 573 K. Hydrogen/glycerol molar ratio of 10 was used in all experiments. Typically 100 mg of sample in the form of pellets, with size ranging 2–3 mm, were loaded in the quartz reactor and the reactor was heated to the desired temperature. The condensed products were trapped in a ice bath condenser and analyzed by HPLC every 20 min of reaction in a high performance liquid chromatography (HPLC, Agilent technologies 1100 series) equipped with a ICsep ICE-COREGEL 87H3 Column serial N° 12525124 column, a diode-array detector (DAD) and a refractive index (RID) detector. The mobile phase was deionized and filtered water with pH controlled to 2.2 by addition of sulfuric acid with flow of 0.6 mL/min and a pressure of 50 bar. The temperature of the HPLC column was 313 K and 50 min of analysis for each chromatogram.

The gaseous products were continuously analyzed by an on-line gas chromatograph equipped with a FID detector and a HP Poraplot column (30 m × 0.53 mm × 0.6 m). Finally, a total organic carbon (TOC) analyzer was used to check the carbon balance. The TOC analysis was performed on a Shimadzu TOC-5000A using high purity air (pressure of 400–500 kPa and flow rate of 150 mL/min) and a furnace temperature of 953 K. The conversion of the glycerol was defined as follows:

$$\text{Conversion of glycerol (\%)} = \frac{\text{Moles of glycerol reacted}}{\text{Initial moles of glycerol}} \times 100$$

The selectivity to each product was defined as selectivity based on carbon, where:

$$\text{Selectivity (\%)} = \frac{\text{Moles of carbon in specific product}}{\text{Moles of carbon in all products}} \times 100$$

In order to understand the glycerol reaction pathways, catalytic conversion of hydroxyacetone, pyruvaldehyde, lactic acid and EG was also carried out in the same operation conditions used for conversion of glycerol. Sample Ni723 was chosen as the representative sample for the catalytic tests to track the reaction pathways. In addition, catalytic conversion of glycerol in inert atmosphere (Ar flow) was realized to evaluate the dehydrogenation and dehydration steps.

2.4. Catalyst regeneration

The Ni723 sample was chosen as a representative material for regeneration test. After 6 h of reaction the Ni723 sample was regenerated in air flow (50 mL/min) from RT to 723 K at 5 K/min and kept at 723 K for 4 h. The catalyst was then purged with Ar flow and reduced under H_2 flow at 723 K for 4 h. The regeneration process was applied in four reaction cycles.

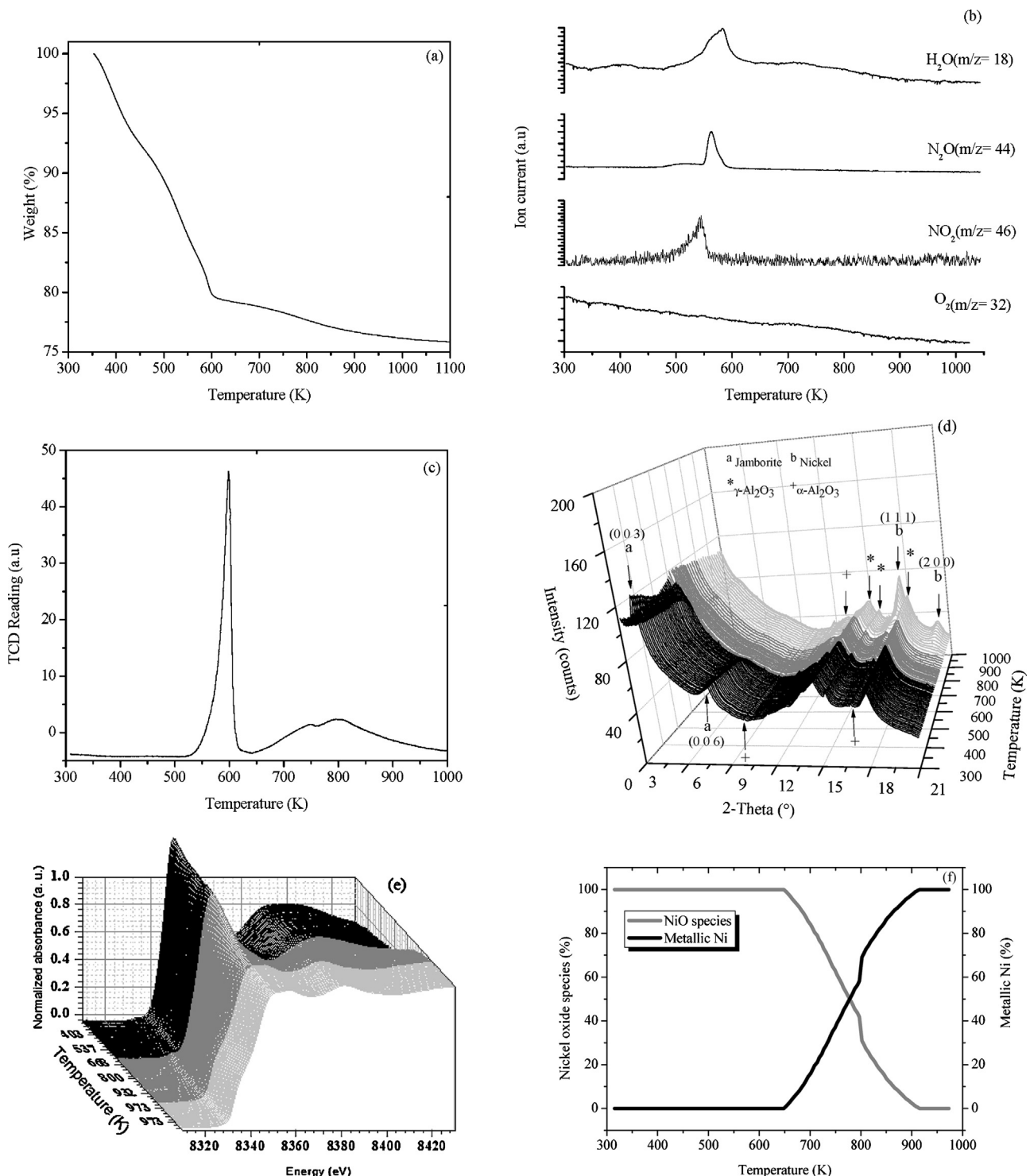


Fig. 1. Thermal decomposition of nickel (II) nitrate hexahydrate impregnated on γ -Al₂O₃: (a) thermogravimetric analysis; (b) MS results obtained from the off gas during thermal treatment, (c) H₂-TPR analysis, (d) XRD *in situ*, (e) XANES and (f) degree of reduction of Ni.

3. Results and discussion

3.1. Catalyst characterization

3.1.1. Thermal decomposition of $\text{Ni}(\text{NO}_3)_2 \cdot 6\text{H}_2\text{O}$ impregnated over γ -Al₂O₃

The $\text{Ni}(\text{NO}_3)_2 \cdot 6\text{H}_2\text{O}$ impregnated over γ -Al₂O₃ sample was characterized by TGA-MS, *in situ* XRD and XANES, as shown in Fig. 1. The main decomposition of $\text{Ni}(\text{NO}_3)_2 \cdot 6\text{H}_2\text{O}$ under H₂/Ar

occurred below 620 K with a constant release of water between 350 and 550 K and intense evolution of water between 550 and 620 K ($m/z=18$). Furthermore, the presence of N_2O ($m/z=44$) and NO_2 ($m/z=46$) between 520 and 620 K, as well as some traces of oxygen ($m/z=32$), were also observed (Fig. 1a and b). The evolution of gases was also monitored by TCD (Fig. 1c). A sharp evolution of hydrogen consumption was observed between 520 and 620 K which corresponds to the decomposition of nickel nitrate precursor to the nickel oxide species, in accordance with

previous work [32,36–38]. In addition, a broad band between 600 and 1000 K (Fig. 1c) is probably due to the reduction of nickel oxide species to metallic Ni. Fig. 1(d) shows the XRD patterns of the impregnated $\text{Ni}(\text{NO}_3)_2 \cdot 6\text{H}_2\text{O}$ over $\gamma\text{-Al}_2\text{O}_3$ reduced *in situ* under a flow of H_2 . Two prominent reflections which could be assigned to $(\text{Ni}(\text{OH})_2(\text{NiOOH})_{0.167})_{0.857}$ (Jamborite, ICDD 89-7111) are evident in the diffractogram when the dried sample was heated from RT to about 600 K. These two peaks correspond to the (003) and (006) planes of the Jamborite phase. Indeed, Sietsma et al. [37] observed that nickel nitrate hydroxide with composition $\text{Ni}_3(\text{NO}_3)_2(\text{OH})_4$ was formed on SBA-15 that had been impregnated with $[\text{Ni}(\text{OH}_2)_6](\text{NO}_3)_2$ aqueous solution. Consequently, the presence of other nitrate phases not detected by XRD should not be discarded. Thus, *in situ* XRD showed that the total decomposition of the Jamborite phase occurred around 600 K in agreement with TGA-MS and TPR. The broad peaks in the TPR profile (Fig. 1c) between 600 and 1000 K indicate the reduction of the NiO species with different interaction with the support [38–40]. The broad TPR signal with a shoulder at 740 K can be attributed to reduction of NiO species which are weakly bound to the $\gamma\text{-Al}_2\text{O}_3$, while the shoulder at around 800 K should be assigned to reduction of NiO species with strong interaction with the $\gamma\text{-Al}_2\text{O}_3$ (Fig. 1c). The Ni K-edge temperature resolved XANES spectrum and the distribution of Ni species with temperature for the *in situ* reduction of $\text{Ni}(\text{NO}_3)_2 \cdot 6\text{H}_2\text{O}$ impregnated over $\gamma\text{-Al}_2\text{O}_3$ are shown in Fig. 1e and f, respectively. The white line (WL) is not affected by the increase in temperature between RT and 650 K, indicating no reduction of Ni oxide to metallic Ni. Between 650 and 920 K, the WL decreases with increasing temperature, indicating formation of metallic Ni. The WL intensity keeps constant above 920 K, suggesting that all Ni oxide was converted to metallic Ni. The XRD patterns (Fig. 1d) show peaks for metallic Ni above 800 K, corresponding to planes (111) and (200) (ICDD 4-0850). The XRD measurements also revealed reflections corresponding to $\alpha\text{-Al}_2\text{O}_3$ (ICDD 46-1212).

Based on TGA-MS, TPR, XANES and *in situ* XRD, we conclude that decomposition of $\text{Ni}(\text{NO}_3)_2 \cdot 6\text{H}_2\text{O}$ impregnated over $\gamma\text{-Al}_2\text{O}_3$ occurred between 350 and 620 K with formation of Ni oxide species, which are finally reduced to metallic Ni between 650 and 920 K. In addition, TGA result shows that total weight loss for the sample was close to the theoretical value of 26.5% for complete decomposition of $\text{Ni}(\text{NO}_3)_2 \cdot 6(\text{H}_2\text{O})$ into metallic Ni [41,42]. The formation of metallic Ni by reduction of Ni oxide species obtained by XANES is represented in Fig. 1f, reaching 100% of reduction above 920 K.

3.1.2. N_2 -physisorption

The N_2 -physisorption results of the samples are depicted in Table 1. The $\gamma\text{-Al}_2\text{O}_3$ support presents a surface area of $113 \text{ m}^2/\text{g}$ and pore volume of $0.20 \text{ cm}^3/\text{g}$. The introduction of Ni on the $\gamma\text{-Al}_2\text{O}_3$ produces a decrease in the surface area of the support and pore volumes, suggesting that the impregnation with Ni species presumably lead to partial pore blockage in the support by Ni species crystallites [38]. For instance, the Ni623 sample presented a surface area of $100 \text{ m}^2/\text{g}$ and pore volume of $0.17 \text{ cm}^3/\text{g}$ against $113 \text{ m}^2/\text{g}$ and $0.2 \text{ cm}^3/\text{g}$ of the $\gamma\text{-Al}_2\text{O}_3$. Additionally, as the reduction temperature pre-treatment of the 10%Ni/ $\gamma\text{-Al}_2\text{O}_3$ samples is increased there is a decrease in surface area from 113 to $74 \text{ m}^2/\text{g}$ compared with the pure $\gamma\text{-Al}_2\text{O}_3$ support, as shown in Table 1. The effect of the reduction temperature on the surface area is remarkable in the Ni993 and Ni1073 samples. All Ni catalysts exhibited the typical type IV isotherms according to the Brunauer–Deming–Deming–Teller (BDDT) classification, which exhibited the condensation and evaporation step commonly found in mesoporous materials. All isotherms at low equilibrium pressures are reversible, whereas, at higher equilibrium pressures, they exhibit a hysteresis loop of the H3 type [43]. This type of hysteresis

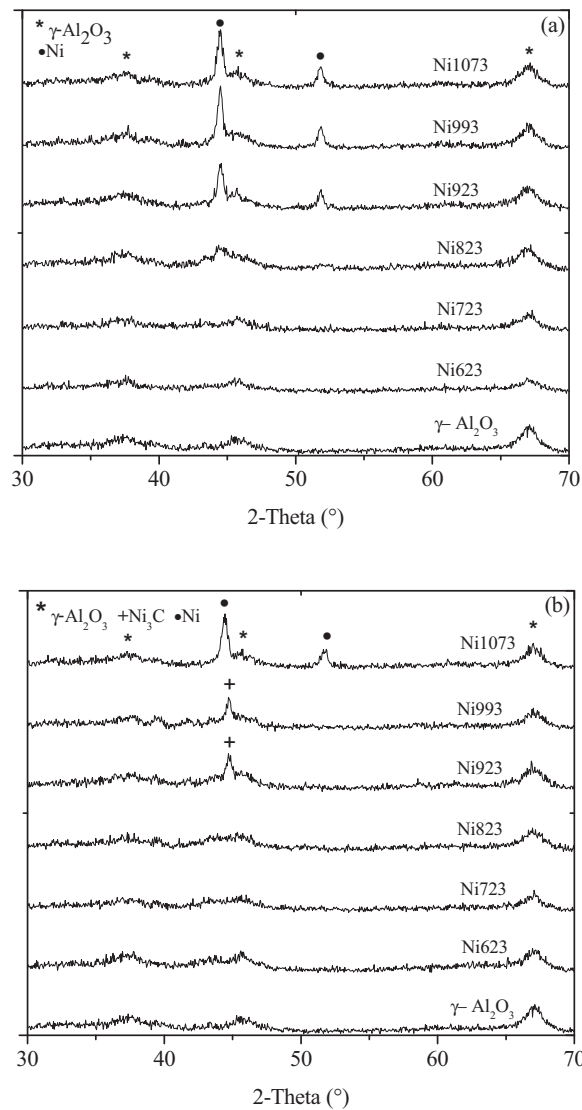


Fig. 2. X-ray diffraction patterns. (a) Fresh and (b) spent supported Ni catalysts.

loop indicates the presence of slit-shaped mesopores or pores with narrow necks and wide bodies.

3.1.3. Conventional X-ray diffraction

The XRD patterns of fresh 10%Ni/ $\gamma\text{-Al}_2\text{O}_3$ samples are shown in Fig. 2a. Two distinct crystallographic phases are observed, which correspond to metallic Ni, and the corresponding $\gamma\text{-Al}_2\text{O}_3$ phase (ICDD 79-1558) of the support. In these diffractograms, the $\alpha\text{-Al}_2\text{O}_3$ phase was not observed, probably due to the low concentration of this phase and the smaller brilliance of the diffractometer. The NiO phase (Bunsenite, ICDD 47-1049) was not detectable in any samples. It can be seen that the metallic Ni diffraction peaks are broad and of low intensity, indicating that the Ni metal particles are highly dispersed on the $\gamma\text{-Al}_2\text{O}_3$ support in the fresh catalysts. The peaks at around $2\theta = 37.5^\circ$, 45.7° and 66.7° are assigned to the $\gamma\text{-Al}_2\text{O}_3$ phase. The other broad peaks at around $2\theta = 44.5^\circ$ and 51.8° are associated with metal Ni phase [38,44], which are observed for samples treated above 823 K. The highest intensity peak observed at the $2\theta = 44.5^\circ$ is attributed to Ni (111) and the peak at $2\theta = 51.8^\circ$ corresponds to Ni (200). It is noteworthy that the metallic Ni peak became more intense as the reduction temperature increased, indicating increase in the Ni particle size by

Table 1

Textural properties of fresh and used catalysts.

Sample	Fresh			Used		
	S_{BET} (m ² /g)	Pore volume (cm ³ /g)	Pore size (nm)	S_{BET} (m ² /g)	Pore volume (cm ³ /g)	Pore size (nm)
$\gamma\text{-Al}_2\text{O}_3$	113	0.20	4.54	–	–	–
Ni623	100	0.17	4.54	89	0.13	4.15
Ni723	99	0.17	4.54	99	0.15	4.54
Ni823	94	0.18	4.75	95	0.17	4.54
Ni923	93	0.19	4.75	91	0.18	4.75
Ni993	79	0.18	5.44	71	0.16	5.44
Ni1073	74	0.17	5.44	70	0.15	5.44

sintering. The spinel NiAl_2O_4 crystalline phase (ICDD 10-339) was not detected in any sample by XRD.

3.1.4. TEM

The morphology and the metal particle size of the fresh 10%Ni/ $\gamma\text{-Al}_2\text{O}_3$ catalysts were characterized by TEM (Fig. 3a). The particle size was measured directly from TEM images at different randomly selected regions for each sample. It can be seen that the shape and density of Ni crystallites distributed over $\gamma\text{-Al}_2\text{O}_3$ changed with the pre-treatment temperature. The Ni particle size distributions of the catalysts are shown in Fig. 3b. The Ni catalyst reduced at 723 K contains small Ni particles with sizes ranging between 4 and 10 nm. As the reduction pre-treatment temperature increased, the Ni particles become larger, with mean diameter at about 10 nm and 20 nm for samples Ni823 and Ni993, respectively. However, when temperature was further increased, larger Ni particles (about 30 nm) with a broader size distribution were observed.

3.1.5. H_2 -chemisorption

Table 2 shows the number of exposed Ni atoms and the percentage of exposed Ni atoms, as determined by H_2 -chemisorption. The Ni623 sample has fewer exposed Ni atoms than the Ni723 sample (3.4% and 33%, respectively), suggesting that Ni species present in the first sample was slightly reduced due to low reduction temperature, in agreement with XANES and TPR results. On the other hand, a loss of exposed Ni atoms is observed with increasing reduction temperature from 723 K to 1073 K (Table 2). The Ni1073 sample shows the lowest percentage of exposed Ni (around 0.7%). A plausible explanation is that sintering is extensive at high reduction temperatures [40,45]. The sintering of Ni particles on alumina is correlated to the bond strength between the metal particle and the support.

3.1.6. NH_3 -TPD

The NH_3 -TPD for the fresh catalysts showed two main desorption regions, at 350–550 K and at 550–900 K, indicating the existence of two kinds of regions having different acid strengths (Table 2). The lower desorption temperature region is attributed to desorption of NH_3 bridge-bound to penta-coordinated aluminum (weak Lewis acidic sites), while the higher temperature region to desorption of terminally bound NH_3 on tri-coordinated aluminum (strong Lewis acid sites) [44].

NH_3 -TPD analysis was also carried out on $\gamma\text{-Al}_2\text{O}_3$ submitted to the different temperature reduction pre-treatments employed for each catalyst. The alumina support also revealed the presence of the two desorption temperature regions attributed to weak and strong acid Lewis sites. The NH_3 desorbed values for the support are very similar, regardless the reduction temperature used. A slight decrease of the strong Lewis acid sites is observed at higher reduction temperatures. However, the Ni incorporation produces a strong increase in the strong Lewis acid sites, mainly for the Ni623 sample. This is probably due to the presence of some Ni oxide and

nitrogen oxide species produced during the decomposition of the nickel nitrate. In general, the introduction of Ni species increased the total acidity compared with the correspondent bare alumina.

The amounts of desorbed NH_3 measured by volumetric adsorption are depicted in Table 2 for all the samples. The surface acidity was calculated as total acidity and expressed per μmol of NH_3 desorbed per gram of sample.

3.2. Conversion of glycerol

The catalytic performance of 10%Ni/ $\gamma\text{-Al}_2\text{O}_3$ catalysts submitted to different reduction temperatures were evaluated in the conversion of glycerol under atmospheric pressure and 573 K. Blank tests using the same reaction conditions and either an empty or charged reactor with $\gamma\text{-Al}_2\text{O}_3$ showed no glycerol conversion. This suggests that neither the homogeneous gas phase glycerol decomposition nor the $\gamma\text{-Al}_2\text{O}_3$ support contributed to the observed activity of the Ni catalyst. Markedly low activity for glycerol reaction was observed when the 10%Ni/ $\gamma\text{-Al}_2\text{O}_3$ sample was calcined without reduction.

The main products in the condensable phase observed during conversion of glycerol were: hydroxyacetone, pyruvaldehyde, pyruvic acid, lactic acid, lactide, ethylene glycol (EG), acetaldehyde, methyl lactate, traces of different products such as 1,2-propanediol (1,2-PDO), methyl pyruvate, acetone, propanal, 2-propanol (2-PO), 1-propanol (1-PO), methanol, formic acid, acetic acid, and furan derivatives. Previous works about glycerol conversion reported that the furan compounds are the result of a catalytic cyclisation of hydroxyacetone [46]. The major products detected in the gas phase were methane (CH_4), acetaldehyde, and traces of formaldehyde, propanal and acetone.

The main products formed can be classified into two main groups: compounds with 3 carbon atoms (C_3) and lower ($C < 3$). In the first group, dehydration and dehydrogenation products such as hydroxyacetone, pyruvaldehyde, pyruvic acid, lactic acid and lactide, are obtained. In addition some lactide (C_6) is formed by dimerization of lactic acid. The other group can be attributed to hydrogenolysis products ($C < 3$) such as CH_4 and acetaldehyde. Methyl lactate and methyl pyruvate were also formed, probably by esterification reaction between methanol with pyruvic acid and lactic acid, respectively. Methanol is formed in the glycerol hydrogenolysis step.

The effect of bifunctional metal–acid properties of the catalysts can be seen in two main routes presented in Scheme 1: (i) the hydrogenolysis of glycerol to methane and acetaldehyde and (ii) dehydration–dehydrogenation to the production of hydroxyacetone, pyruvaldehyde, pyruvic acid, methyl lactate and lactide. In the case of glycerol hydrogenolysis, the number of exposed Ni atoms determined the production of methane and acetaldehyde. The metal property is remarkable especially to the Ni723 sample which presents the highest number of exposed Ni atoms of 3.43×10^{19} (Table 2), inducing the presence of the hydrogenolysis route. On the other hand, the acid property is remarkable especially for the Ni623

Table 2Physical–chemical properties of 10%Ni/γ-Al₂O₃ samples and percent of methane generated after 6 h of reaction.

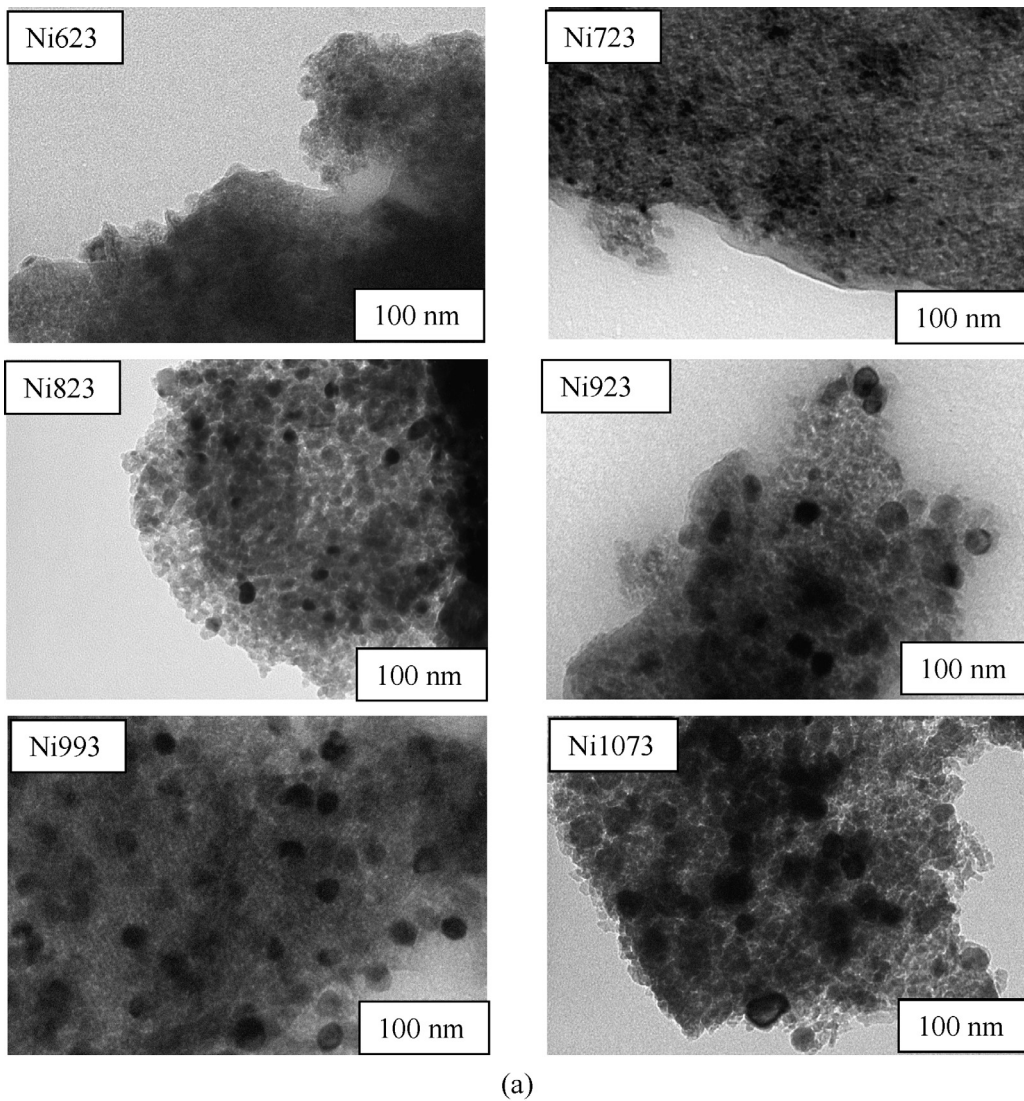
Support	TPD-NH ₃ (μmol/g _{sample})	Sample	Fresh			Number of exposed Ni atoms	XANES	TEM ^a (nm)	Used				
			TPD-NH ₃ (μmol/g _{sample})										
			Total	350–550 K	550–900 K								
γ-Al ₂ O ₃ 623	160.8	35.4	125.4	Ni623	273.1	42.7	230.4	3.53×10^{18} (3.4%) ^b	100 0 1.4 5.97				
γ-Al ₂ O ₃ 723	181.8	47.2	134.6	Ni723	205.4	69.6	135.9	3.43×10^{19} (33%) ^b	75.1 24.9 6.0 5.75				
γ-Al ₂ O ₃ 823	174.0	46.5	127.6	Ni823	198.8	68.7	130.2	1.28×10^{19} (12%) ^b	22.4 77.6 9.0 1.88				
γ-Al ₂ O ₃ 923	168.6	42.9	125.7	Ni923	159.5	37.0	122.5	7.11×10^{18} (6.9%) ^b	0 100 19.0 1.69				
γ-Al ₂ O ₃ 993	157.0	47.0	110.0	Ni993	185.0	66.5	118.6	6.40×10^{18} (6.2%) ^b	0 100 20.0 1.53				
γ-Al ₂ O ₃ 1073	163.4	48.1	115.3	Ni1073	195.3	70.7	124.7	7.67×10^{17} (0.7%) ^b	0 100 25.0 0.74				

^a Mean particle size.^b Values in the brackets are dispersion.

sample which presents the highest acidity (273.1 μmol/g_{sample}, see Table 2) among all samples and it favored the formation of hydroxyacetone and suppressed the formation of methane. Similar to Ni623 sample, the Ni1073 sample also exhibit poor hydrogenolytic capacity but in this case is due to the presence of large Ni particles which conferred the lowest number of exposed Ni atoms with a value of 7.67×10^{17} (Table 2). Even with the progressive increase of the Ni particle size observed above 823 K of reduction temperature, the samples (Ni923 and Ni993) still present similar

CH₄ selectivity values to those obtained for the Ni723 and Ni823 samples. It is important to note that esterification products such as methyl lactate and methyl pyruvate are observed when both routes of hydrogenolysis and dehydration–dehydrogenation are present. Since Ni1073 sample presented the poorest hydrogenolytic capacity, esterification products were not observable.

The catalytic performance for 10%Ni/γ-Al₂O₃ reduced at different temperatures is shown in Fig. 4. It shows a decrease in glycerol conversion with time on stream. The deactivation was more



(a)

Fig. 3. (a) TEM images of the fresh 10%Ni/γ-Al₂O₃ samples reduced at different temperatures and (b) nickel particle size distribution.

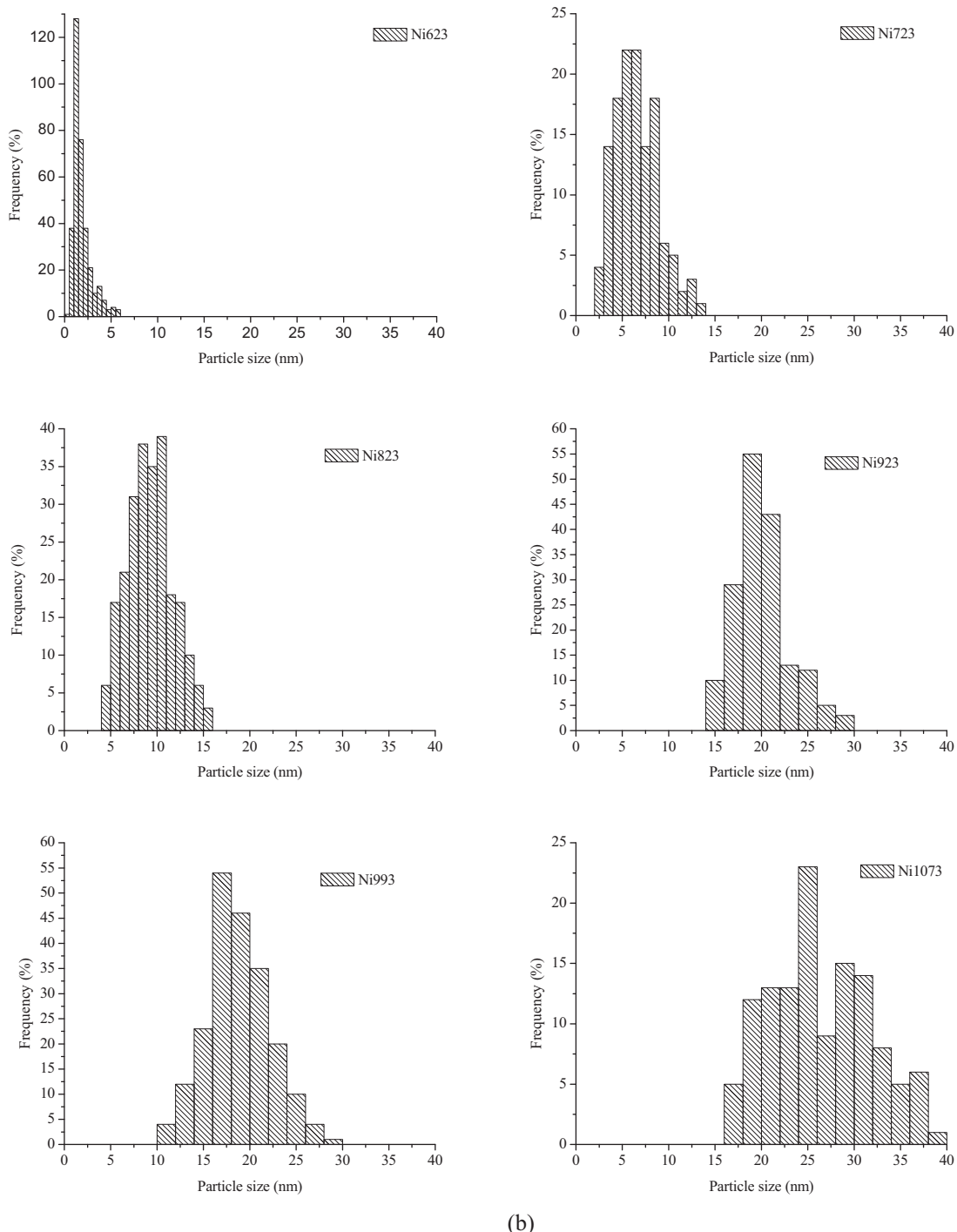
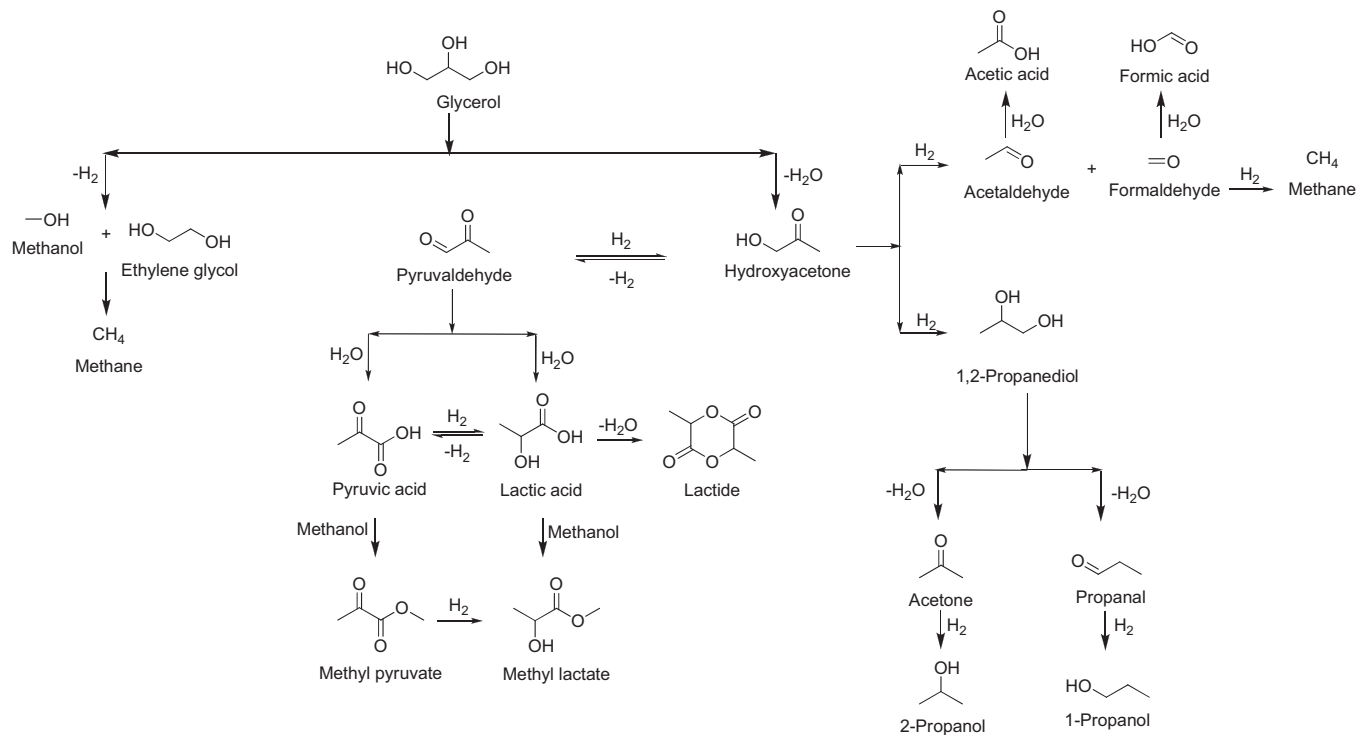


Fig. 3. (Continued).

pronounced for the Ni623 sample. The Ni623 catalyst has the largest amount of stronger Lewis acid sites ($273.1 \mu\text{mol/g}_{\text{sample}}$) and the lowest amount of reduced Ni compared with the other samples (Table 2).

The comparative selectivity profiles of the different products obtained for the Ni623, Ni723, Ni923 and Ni1073 samples are shown in Fig. 5. In general, the Ni623, Ni723 and Ni923 exhibited similar tendency in product distribution. The catalyst deactivation shown in Fig. 4 affected the selectivity during the glycerol conversion, particularly for the Ni623, Ni723 and Ni923 samples. The selectivity to hydrogenolysis products such as CH_4 decreases meanwhile the products of dehydration and dehydrogenation increase.

For all these three catalysts the selectivity to CH_4 is about 100% initially, and then decreases progressively to about 10–20% after 3 h of reaction. Upon raising the reaction time to 6 h, the CH_4 selectivity remains unchanged. The decrease in CH_4 selectivity is accompanied by an increased of other products such as hydroxyacetone, pyruvaldehyde, pyruvic acid, lactide and EG. The selectivity to acetaldehyde increases in the first hours, until eventually reaches a maximum and starts to decrease throughout the reaction. For instance, for the Ni723 sample, the selectivity to hydroxyacetone increased from 10.6% to 15.4% with raising reaction time from 2 h to 4 h. Selectivities, during this period, toward pyruvaldehyde, lactide and acetaldehyde changes from 0% to 6.2%, 14.6% to 27.7% and



Scheme 1. Proposed general reaction pathways for glycerol conversion.

31.5% to 21.3%, respectively. The lower selectivity is to EG, rising to approximately 4% with the increase in reaction time. Considering the selectivity presented by the Ni623, Ni723 and Ni923 at 50% glycerol conversion, the selectivity to hydroxyacetone is 20.1%, 15.1% and 17.4%, respectively, as shown in Fig. 5.

The Ni623 and Ni1073 samples have selectivity values for CH_4 of 8.7% and 3.8%, respectively, which are lower than those obtained for Ni723, Ni823, Ni923 (18.8%, 22.6%, and 13.3%) at 6 h of reaction, respectively (Fig. 5). The Ni623 and Ni1073 present the lower number of exposed atoms with values of 3.53×10^{18} and 7.67×10^{17} , respectively (Table 2). The low selectivity to CH_4 observed for Ni623 sample may be attributed to the low reduction degree of Ni, as shown by H_2 chemisorption and XANES (Table 2) and larger Ni particles in the case of the Ni1073 (Table 2). The

increase in the reduction temperature pre-treatment modulates the degree of reduction and sintering of the Ni species affecting the hydrogenolytic capacity of the Ni samples. Table 2 shows that Ni723 and Ni823 samples have the higher number of exposed Ni atoms, respectively, leading to higher hydrogenolytic capacity. Indeed the Ni723 sample has the lowest selectivity to pyruvaldehyde at 6 h of reaction, due to its higher hydrogenolytic capacity. At the same time, as noted in Table 2 by XANES analysis, the percentage of NiO progressively decreases with the reduction temperature and above 920 K Ni particles are totally reduced. Even with the progressive decrease in the number of exposed Ni atoms observed above 823 K, the Ni923 and Ni993 samples still presents similar CH_4 selectivity values to those obtained for the Ni723 and Ni823 samples (Fig. 5). The total reduction of Ni species in the Ni923 and Ni993 samples may supply active sites for hydrogenolysis at the expense of the loss in the number of exposed Ni atoms. However, further increase in the reduction temperature above 1000 K causes extensive sintering of the Ni particles as revealed by the TEM results (Fig. 3 and Table 2), becoming less selective to CH_4 . Indeed markedly behavior is found for the Ni1073 sample, as shown in Fig. 5d, which exhibits a stable product distribution with time-on-stream and absence of deactivation.

The deactivation strongly influences the product distribution with time-on-stream during the glycerol conversion. There is a compromise between the reduction temperature pre-treatment employed with stability and catalytic performance. Previous works [36,38] have reported deactivation in the glycerol hydrogenolysis reaction attributing it to a number of factors like oxidation of metallic species promoted by the presence of water, sintering of the active metallic phase, and presence of carbon species on the catalytic surface.

3.3. Reaction pathway

Hydroxyacetone, pyruvaldehyde, lactic acid and EG were used as reactants under the same operation conditions performed for the

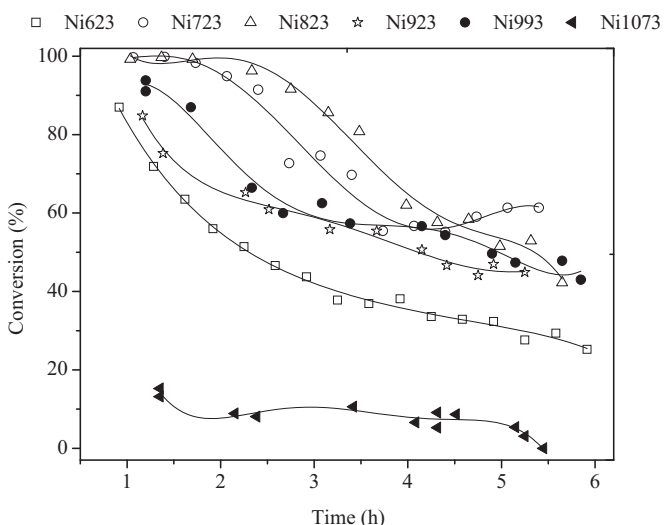


Fig. 4. Catalytic performance of the 10%Ni/γ-Al₂O₃ samples in function of time of reaction.

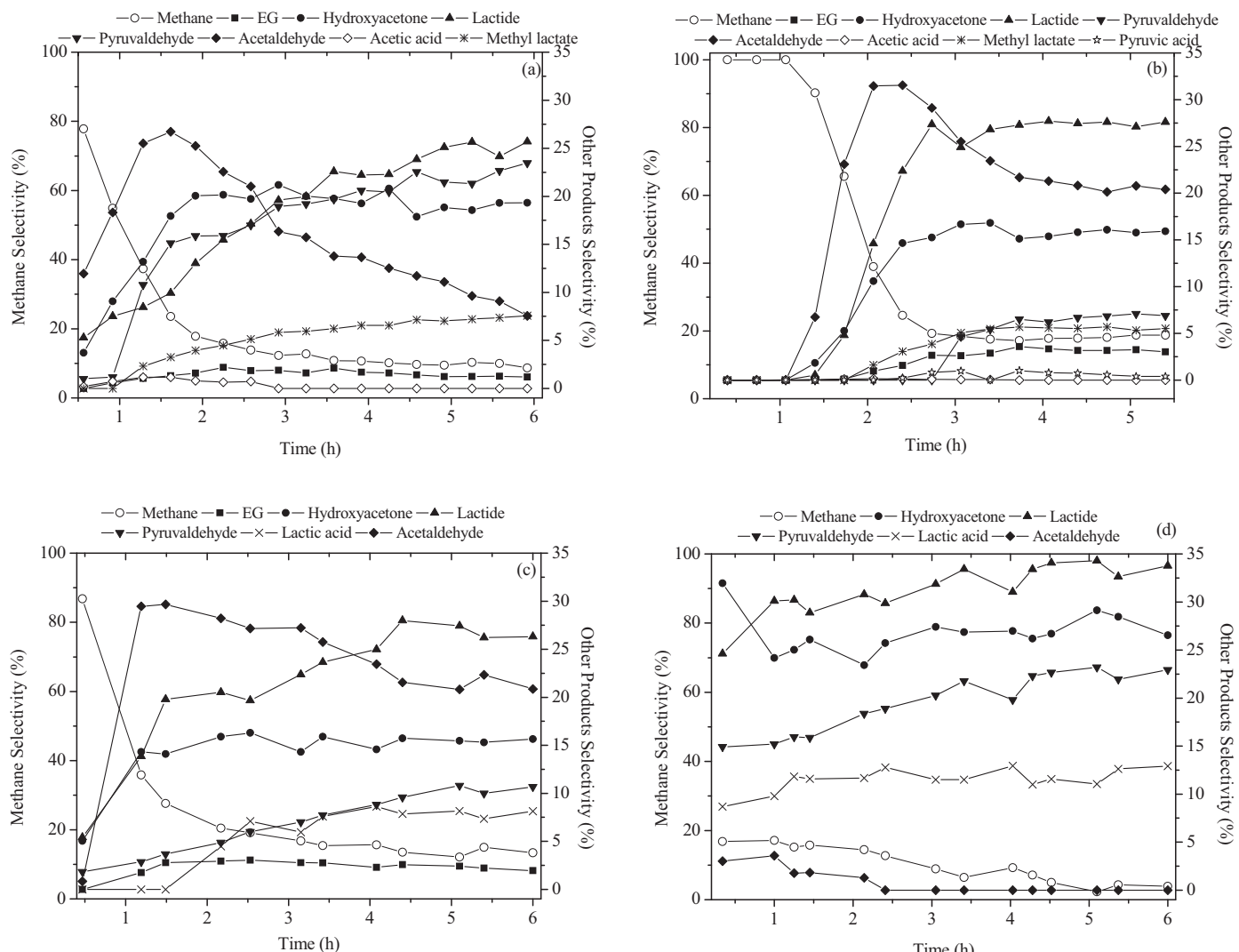


Fig. 5. Time-on stream product selectivity in glycerol conversion over Ni623, Ni723, Ni923 and Ni1073.

catalytic conversion of glycerol in order to investigate the reaction pathway. The conversion and selectivity obtained during catalytic tests of glycerol, hydroxyacetone, pyruvaldehyde, lactic acid and EG at 4 h of reaction are shown in Table 4 for the sample Ni723.

The glycerol conversion found at 4 h of reaction was about 57% (column 2, Table 4). Acetaldehyde, EG, hydroxyacetone, lactic acid, lactide, methane, pyruvaldehyde, methyl lactate and pyruvic acid were the main products, with respective selectivities at 4 h of 21.3%, 3.3%, 15.4%, 1.9%, 27.7%, 17.8%, 6.2%, 5.6% and 0.8%. Traces of furan derivatives were also detected in the liquid products.

In addition, we have also studied the conversion of glycerol using the Ni723 catalyst under argon flow (column 3, Table 4). The conversion under Ar atmosphere was slightly lower than that observed under H₂ flow as shown in Table 4 (46% and 57%, respectively). The products were similar to those obtained under H₂ atmosphere, however an increase in the selectivity to lactic acid, lactide, pyruvaldehyde and methyl lactate was observed, mainly at expenses of acetaldehyde and CH₄. This indicates that the dehydration and dehydrogenation routes prevail over the hydrogenolysis route.

The total suppression of CH₄ formation was clearly observed when the Ni catalyst was previously calcined at 723 K instead of reduced as shown in Table 4 at column 4. Starting with the Ni catalyst at oxidized state the conversion is very low (9%) at 4 h

of reaction whereas hydroxyacetone, lactic acid, lactide and pyruvaldehyde were the main products. Methane and acetaldehyde formation were completed suppressed, suggesting that dehydration and dehydrogenation routes can occur on oxidized Ni while hydrogenolysis are favored on metallic Ni.

The main products obtained when hydroxyacetone was employed as reactant (column 5, Table 4) were lactic acid, lactide, acetaldehyde and CH₄. Based on previous works the acetaldehyde and the CH₄ can be obtained from the catalytic C–C bond cleavage of hydroxyacetone [47]. The hydroxyacetone can also be dehydrogenated toward pyruvaldehyde, which finally may give lactic acid (LA) by an intramolecular Cannizzaro reaction [48] and lactide, which is a cyclic dimer obtained from lactic acid.

Hydroxyacetone, lactic acid, methyl lactate, pyruvic acid, acetic acid, acetaldehyde and CH₄ were the major products during catalytic conversion of pyruvaldehyde with correspondent selectivity of 13.2%, 15.2%, 30.3%, 10.1%, 5.4%, 16.1% and 9.7% (column 6, Table 4). These results suggest that hydroxyacetone may be formed not only from direct dehydration of glycerol but also from the hydrogenation of pyruvaldehyde.

When lactic acid was employed as reactant (column 7, Table 4), the main products obtained were hydroxyacetone, lactide, pyruvic acid, acetic acid, acetaldehyde and CH₄. Concerning the

products from EG (column 8, **Table 4**), the only product observed was CH₄. The most severe deactivation was reached when the hydroxyacetone was used as test molecule, showing a conversion of 16% at 4 h of reaction.

Taking into account all the previously catalytic results stated in **Table 4**, we were able to propose a pathway for glycerol conversion (**Scheme 1**). Glycerol is consumed by dehydration reaction to form hydroxyacetone. The hydroxyacetone is dehydrogenated to form pyruvaldehyde. Our results show that pyruvaldehyde can be hydrogenated to form hydroxyacetone, which is hydrogenated in a trace level toward 1,2-PDO. The formation of 1,2-PDO by the metal–acid bifunctional catalyst system is explained by the mechanism where the acid function plays a role of dehydration reaction and the metal catalyzes the hydrogenation reaction [48]. On the other hand, pyruvaldehyde can be converted to lactic acid either *via* a Cannizzaro reaction [48] or *via* oxidation to pyruvic acid which can further hydrogenate forming lactic acid in a reverse reaction. Finally the lactic acid undergoes dimerization to form lactide. Additionally, the pyruvic acid can esterify with methanol forming methyl pyruvate in a minor level. Methyl lactate was also detected that can be produced by esterification between methanol and lactic acid. Methanol is formed in the direct hydrogenolysis step of the glycerol. The methyl pyruvate can also hydrogenate to methyl lactate.

We could not detect 3-hydroxypropanal, 1,3-PDO and acrolein in our experimental conditions. The preferable formation of hydroxyacetone to 3-hydroxypropanal is probably due to the thermodynamic stability of hydroxyacetone [29]. Another route observed in the glycerol conversion was related to EG formation. However, EG was not detected in the experiments when hydroxyacetone, pyruvaldehyde and lactic acid were reactants, suggesting that EG was formed by direct hydrogenolysis of glycerol. Methane and acetaldehyde were also obtained in the glycerol conversion reaction. Methane can be obtained by progressive steps of hydrogenation of pyruvaldehyde and hydroxyacetone, and simultaneously also by direct hydrogenolysis of glycerol. Methanol was observed at trace level, which may be produced from the direct hydrogenolysis of glycerol, undergoing degradation toward CH₄ and esterification of pyruvic acid and lactic acid forming methyl pyruvate and methyl lactate, respectively.

Both CH₄ and acetaldehyde were also obtained when hydroxyacetone, pyruvaldehyde and lactic acid were used as reactants. The acetaldehyde may be obtained from the C–C cleavage of the hydroxyacetone as has been already mentioned by previous works [47]. Acetaldehyde afterwards was oxidized in minor extension to acetic acid. Traces of formaldehyde and formic acid were also detected, which may come from the cleavage of hydroxyacetone. Formic acid is formed by oxidation of formaldehyde. Acetone and propanal were also detected as trace products, derived probably by dehydration of 1,2-PDO. The observed traces of 2-propanol and 1-propanal may originate during the hydrogenation of acetone and propanal, respectively.

3.4. Used samples

The formation of carbonaceous deposits is an undesired side reaction [49]. It has previously been demonstrated that the deactivation of Ni-supported catalysts by carbon deposits is due to both the presence of carbonaceous residues and of partially dehydrogenated and dehydrated species [38,50]. The deposited carbon may have different structures, orders, morphologies and reactivity depending on reaction conditions and on the structure of the catalyst [51]. Polymeric, filamentous and graphitic carbon can be formed on the catalyst [52,53]. The deactivation of the 10%Ni/γ-Al₂O₃ during the conversion of glycerol can be assigned to a number of factors, as hinted by the characterization of the spent samples.

The textural properties measured by N₂-physisorption for fresh and used catalysts were similar (**Table 1**), suggesting that the deactivation may not be dependent on the changes in surface area, pore volume, and pore size of the catalyst during the catalytic conversion of glycerol.

XRD shows differences between fresh and used catalyst (**Fig. 2a** and b). Only the γ-Al₂O₃ phase was observed in the XRD patterns of the Ni623, Ni723 and Ni823 samples. In sample Ni1073, the Ni metallic phase is also discerned. Nickel carbide (Ni₃C, ICDD 6–697) was observed for the used Ni923 and Ni993 samples (**Fig. 2b**). Previous work [54] observed the formation of nickel carbide during reaction between diethyl ether and hydrogen. Therefore, deactivation observed during glycerol conversion can also be attributed to formation of nickel carbide.

TEM of the samples after reaction revealed no variation in the Ni particle size distribution (**Fig. 6**) with respect to the fresh samples (**Fig. 3**). The sintering process was not observed for the Ni samples during the reaction, suggesting that it was not responsible for the catalyst deactivation.

The amounts of carbon deposition on spent 10%Ni/γ-Al₂O₃ catalysts were determined by TPO and they are shown in **Table 2**. As the reduction temperature of pre-treatment increased, less carbon is formed on the catalyst. The spent Ni623 contained the highest amount of coke (5.97 wt.%) and the spent Ni1073 the lowest (0.74 wt.%). Therefore, TPO and catalytic activity results show that carbon deposition on the catalyst is a source of the observed deactivation. Catalyst deactivation observed during the catalytic conversion of glycerol is due to deposition of carbon species on the surface of the catalyst decreasing greatly the availability of the required active centers and consequently depressing the overall activity [55,56].

The quantification of the total acid sites obtained by NH₃-TPD analysis is expressed in **Table 2**. The Ni623 presents the higher amount of acid sites among all catalysts, as well as the higher amount of carbon deposited on the catalyst, suggesting that the carbon on the catalyst is formed during dehydration reactions on the acid sites. In addition, except for the Ni1073 sample, all catalysts showed high selectivity to CH₄ at the beginning of the reaction (**Fig. 5**), suggesting that glycerol is degraded to form lower-molecular alcohols and gases *via* hydroxyacetone and direct hydrogenolysis of glycerol (**Scheme 1**). Atia et al. [57] observed catalyst deactivation during dehydration of glycerol on heteropolyacid catalysts and they attributed it to the blocking of the catalyst surface by carbon, which was related to the catalyst acidity and pore size. Similarly, Vasiliadou and Lemonidou [22] observed deactivation by carbon during glycerol hydrogenolysis on copper catalysts.

The effect of the total acidity on the catalytic performance must be pointed out, particularly for the Ni623 sample. Its total acidity of 273 μmol NH₃/g_{sample} was the highest one. Indeed, as based on **Fig. 4** it was possible to distinguish that the deactivation for this sample was the most severe among all samples. This sample also has the highest level of carbon deposition (5.97 wt.%) as determined by TPO (**Table 2**). In contrast, the total acidity among the other samples recorded in **Table 2** varied by less than 10%. Although the acid sites contribute to the formation of carbon by the dehydration route, the carbon deposition on the catalyst also depends on the Ni particles size (**Table 2**). Some contribution of metallic Ni to the formation of carbon by hydrogenolysis could be expected. This is remarkable for Ni723 which presents the higher number of exposed Ni atoms. It is well known that carbon deposition is also a consequence of the ability of the Ni to break the C–C bond producing CH₄ by hydrogenolysis reaction. However, larger Ni particles produce lower amount of carbon deposition. The highest reduction temperature employed for the Ni1073 sample induced Ni sintering, resulting in loss of exposed Ni atoms and therefore it decreased the

hydrogenolysis routes and formation of carbon on the catalyst, as can be observed in [Table 2](#). Therefore, Ni particles size plays an important role in the glycerol conversion.

Raman spectroscopy was also performed on the spent catalysts to investigate the carbon formed on the samples. It is known that light absorption by carbon depend on the compounds present in the reaction medium and on the deactivation conditions [\[58\]](#).

Raman spectra in the range of 300–800 cm^{−1} show signals that can be contribution of NiO vibrations, specially for the catalyst Ni623 that shows a peak between 400 and 600 cm^{−1}, and the catalyst Ni723 that shows a peak between 300 and 450 cm^{−1}. In addition, another signal around 730 cm^{−1} is assigned to NiO as it was proved by Mendoza et al. [\[59\]](#). Raman spectra in the high wavenumber region ([Fig. 7](#)) display two bands centered at about 1347 cm^{−1} and 1590 cm^{−1}, which were associated with the defect and graphite modes, e.g., D-band and G-band, respectively [\[60\]](#). According to previous works [\[60–62\]](#), the D-band is associated to the disorder-induced vibration of C–C bond and the G-band is

related to the C–C vibration of the carbon material with a sp² orbital structure. These findings suggest that the carbon species found on the surface of Ni-based catalysts consisted of non-deactivating carbon (amorphous carbon) and deactivating carbon (graphitic carbon), respectively. In addition, Ni₃C formed could be attributed to the fact that the crystalline graphite powder may transform to an amorphous state due to carbon atoms diffusing into the Ni lattice [\[60\]](#). The ratios of the intensities of D and G bands (I_D/I_G) were calculated as the ratio of their peak areas. The results were 1.71, 1.59, 1.41, 2.80, 1.98 and 4.51 for Ni623, Ni723, Ni823, Ni923, Ni993 and Ni1073, respectively, and this indicated that amorphous carbon deposition on the solid is higher. For the samples pre-treated at temperatures above 823 K, the intensity of both bands became weaker. The intensity of these bands correlates well with the amount of deposited carbon determined by TPO.

The XPS and TPO results presented in [Table 3](#) reinforce the evidence of carbon species over Ni and γ -Al₂O₃ used materials. The carbon deposition during the initial time on stream is important

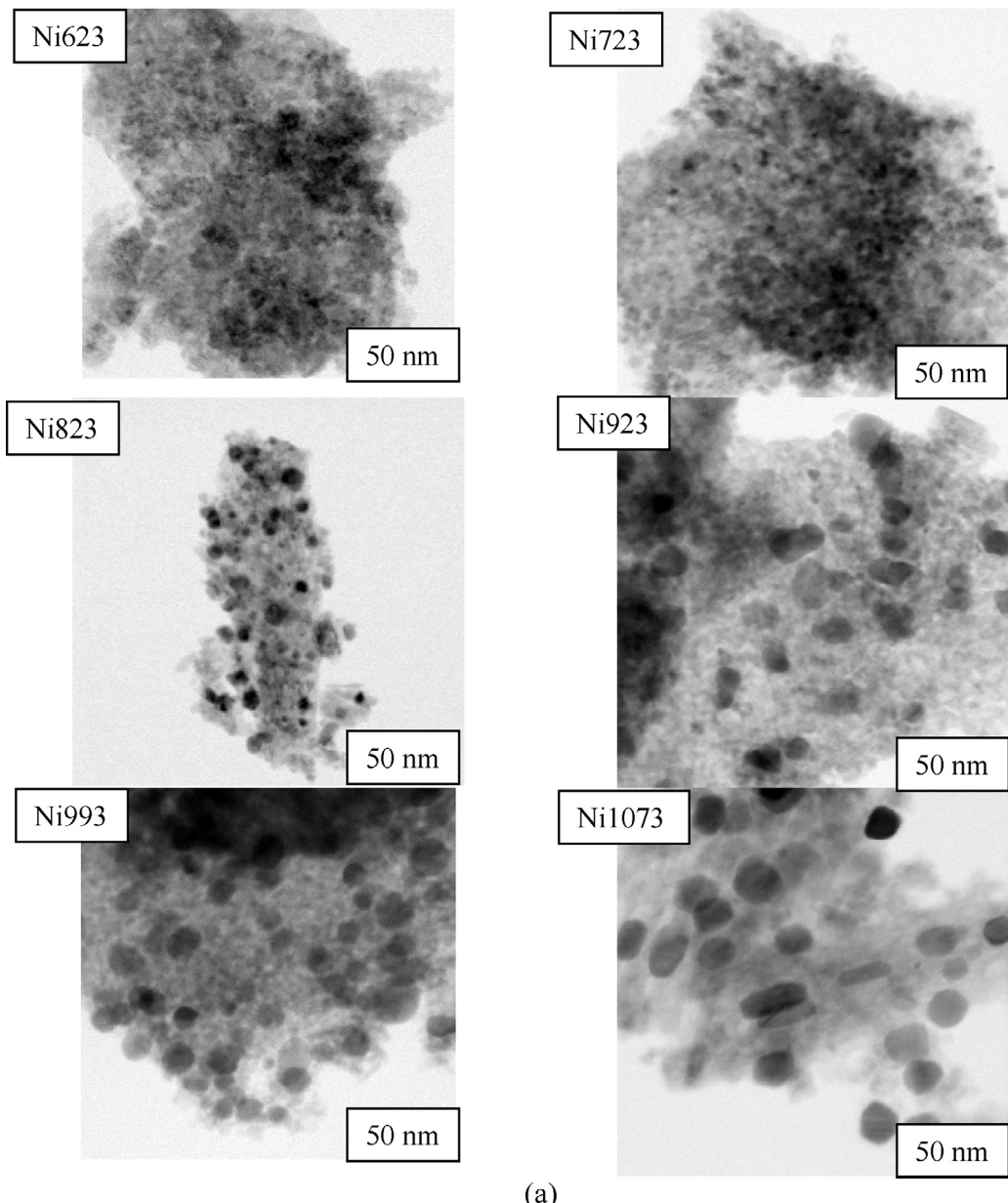


Fig. 6. (a) TEM images of the 10%Ni/γ-Al₂O₃ used samples and (b) nickel particle size diameter distributions of the samples after reaction.

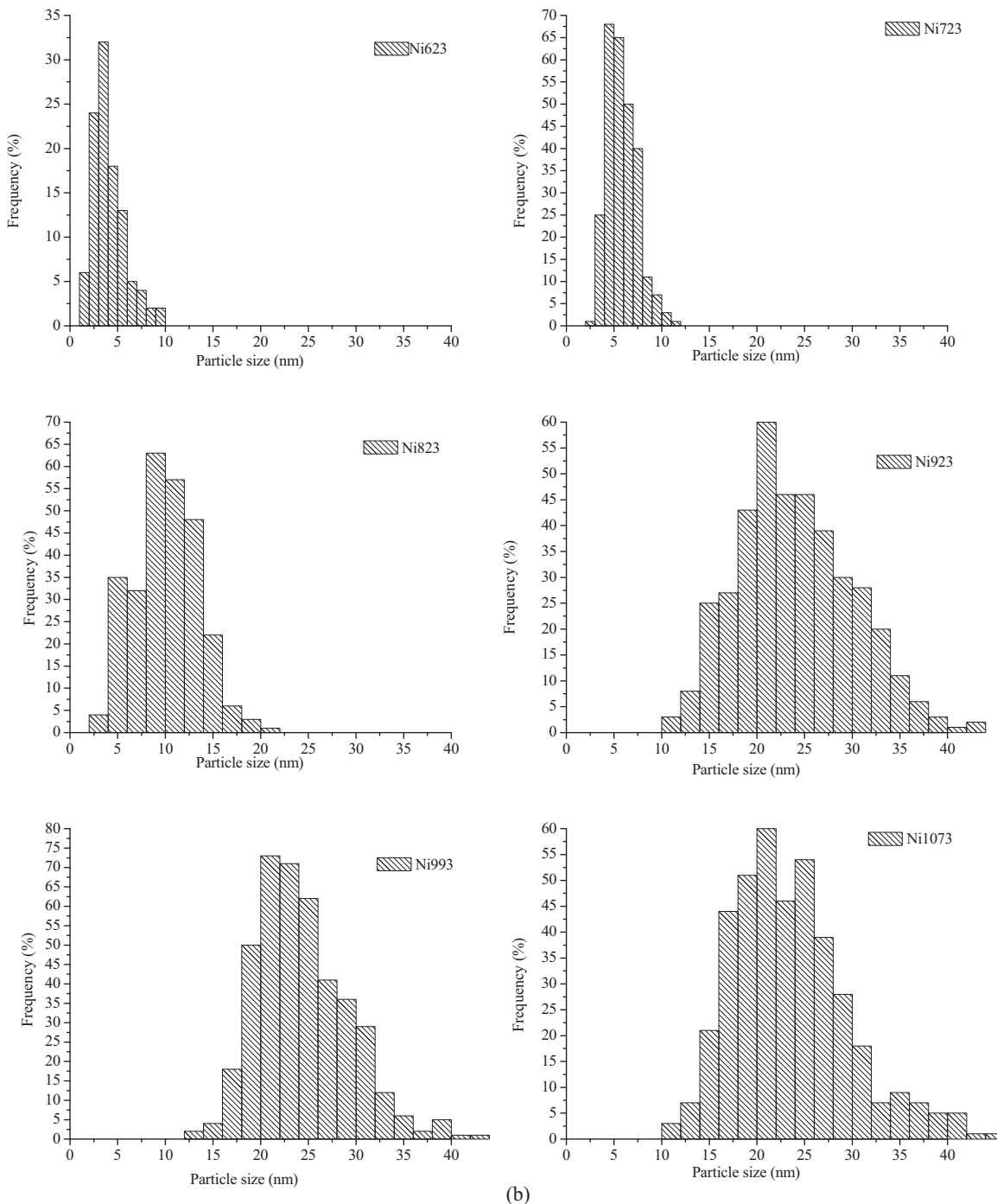


Fig. 6. (Continued).

in the investigation because the catalytic activity greatly decreased during the first 2 h of reaction, as shown in Fig. 4. The effect of time on stream on carbon deposition was investigated for the Ni723 sample in order to get insights into this deactivation process. Carbon deposition was evaluated in different periods of reaction (1 h, 2 h, and 3 h). By comparing the amount of carbonaceous species deposited on the spent catalysts by TPO, it was observed that the Ni723 catalyst had less carbonaceous deposits after 1 h of reaction than 2 h and 3 h, suggesting that the deposit accumulates. As the reaction time increased from 1 h to 6 h, the carbonaceous deposits increased from 3.65 wt.% to 5.75 wt.% (Table 3).

The Ni723 spent sample was also evaluated by XPS to provide information about the oxidation state and chemical environment

of the elements present on the surface of the catalyst (Table 3). During 6 h of reaction, the C/Ni atomic ratio clearly increases, changing from 2.08 after 2 h of reaction to 10 after 6 h of reaction. This indicates a progressive increase in the carbonaceous species over Ni producing some deactivation of the catalyst (Fig. 4). A similar tendency was noted for the C/Al atomic ratio indicating an accumulation of carbonaceous deposits over alumina as the reaction progresses. The Ni/Al atomic ratio increased from the fresh condition compared with the spent catalysts after 6 h of reaction, reinforcing the idea that carbonaceous deposits accumulate more over the surface of the support than over the metal particle.

HRTEM shows that Ni923 sample is composed of 6–10 nm Al_2O_3 crystallites and 15–20 nm Ni-containing particles (Fig. 8a). Both

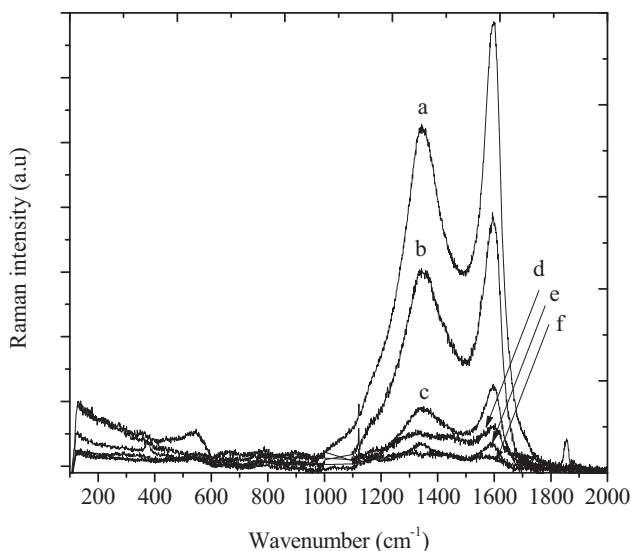


Fig. 7. Raman spectra of the spent catalysts: (a) Ni723; (b) Ni623; (c) Ni823; (d) Ni923; (e) Ni 993 and (f) Ni1073.

Table 3

Surface atomic ratio determined by XPS and TPO analysis of the spent Ni723 sample after different times of reaction.

Time of reaction (h)	Surface atomic ratio by XPS			TPO (wt.% C)
	Ni/Al	C/Ni	C/Al	
0 h	0.13	1.30	0.17	–
1 h	–	–	–	3.65
2 h	0.14	2.08	0.28	4.39
3 h	0.12	3.45	0.40	5.57
4 h	–	–	–	5.21
6 h	0.30	10	2.9	5.75

kinds of particles are crystalline. Lattice-fringe analysis and Fourier Transform (FT) images reveal spots at 1.76 Å and 2.04 Å in particle labeled “a”, which are ascribed to (2 0 0) and (1 1 1) crystallographic planes of metallic Ni, respectively. On the other hand, particle labeled “b” exhibits lattice fringes at 3.50 Å, which are ascribed to (1 1 0) planes of NiO. Therefore, both Ni and NiO phases are present. In some cases these two phases occur in separate particles, but in most cases, however, they appear intimately mixed within the same particle. **Fig. 8b**, for example, shows a particle with highly inhomogeneous contrast. Its FT image reveals the presence of spots

at 2.04 Å and 2.42 Å, which correspond to (1 1 1) crystallographic planes of Ni and NiO, respectively. **Fig. 8b** also shows the occurrence of carbon deposition around this particle. The carbon phase is poorly defined and close to amorphous carbon. Lattice fringes are hardly seen, but a tentative spacing larger than 3.9 Å can be measured (much larger than that of graphitized carbon). Carbon deposition is also evident over the Al₂O₃ support. **Fig. 8(c)** shows a NiO particle exhibiting (1 1 1) crystallographic planes at 2.42 Å (labeled “b”) and lattice fringes at 2.04 Å (labeled “a”), characteristic of the (1 1 1) crystallographic planes of metallic Ni. Exactly the same situation is observed in **Fig. 8d**. In this case, particle “a” corresponds to NiO (spots in the FT image at 2.42 Å), and the small particle labeled “b” attached to it shows the characteristic lattice spacing at 2.04 Å of metallic Ni. A thin layer of carbonaceous deposits is also observed. A last example is depicted in **Fig. 8e**. Again, both NiO and Ni are identified in the same particle. Area labeled “a” shows lattice fringes at 2.04 Å corresponding to (1 1 1) crystallographic planes of metallic Ni, whereas area labeled “b” shows spots at 2.09 Å and 2.42 Å, which are ascribed to (2 0 0) and (1 1 1) crystallographic planes of NiO. Furthermore, **Fig. 9** shows the XPS spectrum for the Ni723 sample after 6 h of reaction. The Ni 2p core-level is composed of two components, Ni 2p_{3/2} and Ni 2p_{1/2} (which result from the spin orbital splitting) and shake up satellites. The Ni 2p_{3/2} core level spectra shows primary satellite peaks around 862.5 eV due to shake-up electrons. Wherever the lines shape of the Ni 2p_{3/2} and Ni 2p_{1/2} peaks were unsymmetrical and broad. In the surface of the Ni723 sample after 6 h of reaction, Ni appears in XPS spectra in two forms: one corresponds to metallic Ni and has the line of Ni 2p_{3/2} level at 852.3 eV and the second form corresponds to ionic nickel (Ni²⁺), with binding energies of about 855.1 eV, due to superficial NiO [63,64]. The oxidation of Ni could be resultant of the reaction conditions (presence of steam at high temperature) as is revealed by HRTEM and XPS and it could be also a source of catalyst deactivation. Bienholz et al. [65] reported a decrease in glycerol conversion on CuO/ZnO and concluded that the water loaded into the reactor or the water formed during the hydrogenolysis deactivated the catalyst.

Carbonaceous deposition is also observed by HRTEM to occur both over the Ni-containing particle as well as over the Al₂O₃ support. Large particles exceeding 30 nm in size are observed. These large particles are difficult to characterize by HRTEM due to their thickness (electron opacity), but at the outer rim it is possible to obtain lattice fringe images. **Fig. 8f** and **g** shows two of these large particles. In **Fig. 8f**, the inset shows the area labeled “a” at high magnification, where it can be observed an excellent crystalline nature. The Fourier Transform image (FT) corresponding to the area “a”

Table 4

Product selectivity in the conversion at 573 K of several main products from the catalytic conversion of glycerol with Ni723 sample at 4 h of reaction.

Column 1	Column 2	Column 3	Column 4	Column 5	Column 6	Column 7	Column 8
Reactant	Glycerol	Glycerol	Glycerol	Hydroxyacetone	Pyruvaldehyde	Lactic acid	EG
Molar ratio H ₂ /reactant	10	0 ^a	10 ^b	10	10	10	10
Conversion (%)	57	46	9	16	71	30	100
Selectivity (%)							
Acetaldehyde	21.3	3.4	–	11.2	16.1	2.0	–
Acetic acid	–	–	–	–	5.4	2.1	–
Ethylene glycol	3.3	–	–	–	–	–	–
Hydroxyacetone	15.4	16.5	29.5	–	13.2	9.1	–
Lactic acid	1.9	6.0	12.2	61.0	15.2	–	–
Lactide	27.7	36.6	35.4	13.7	–	7.1	–
Methane	17.8	9.6	–	14.0	9.7	18.4	100
Pyruvaldehyde	6.2	14.9	22.8	–	–	–	–
Methyl lactate	5.6	12.9	–	–	30.3	–	–
Pyruvic acid	0.8	–	–	–	10.1	61.2	–
Mass balance ^c (%)	91	87	92	90	100	100	100

^a Argon atmosphere.

^b NiO catalyst.

^c TOC, HPLC and CG analysis.

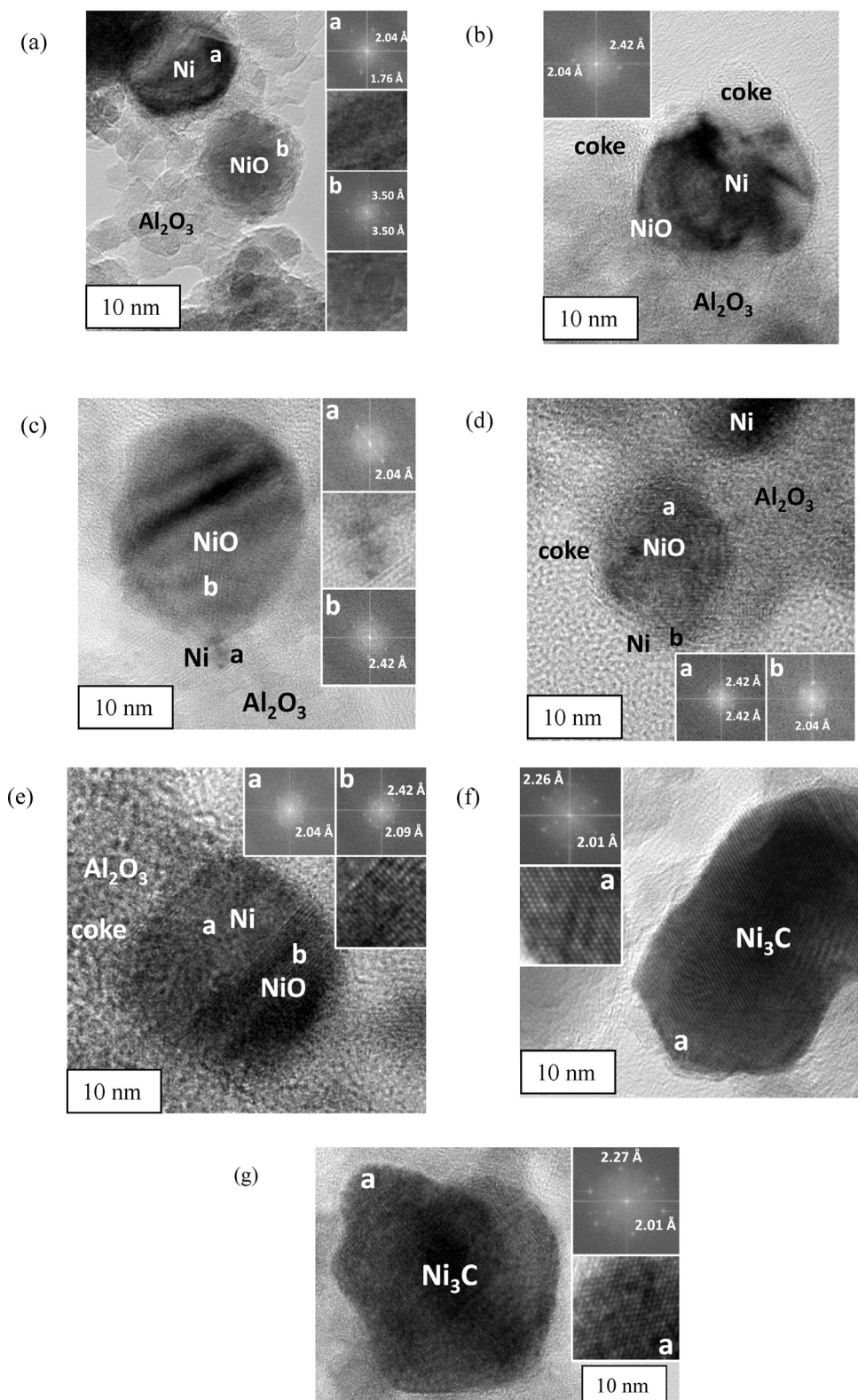


Fig. 8. High resolution transmission electron microscopy image of Ni923 catalyst after reaction. Fourier Transform images are included.

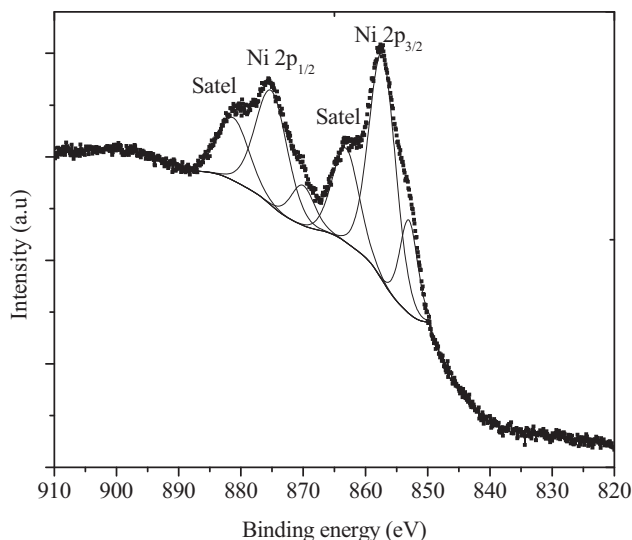


Fig. 9. XPS spectra of Ni723 sample after 6 h of reaction.

shows sharp spots at 2.01 and 2.26 Å, which correspond to (1 1 3) and (1 1 0) crystallographic planes of nickel carbide, Ni_3C . A similar analysis is performed in Fig. 8g. Therefore, there is no doubt that, in addition to small Ni and NiO particles, there are also Ni_3C crystals. These Ni_3C particles are large and very well crystallized, as observed by XRD (Fig. 2b). Ni and NiO particles are less crystalline and smaller, making their analysis by XRD more difficult. By HRTEM, Ni, NiO and Ni_3C are detected.

3.5. Regeneration

The Ni723 sample was used as a representative sample for further studies about the regeneration process as depicted in Fig. 10.

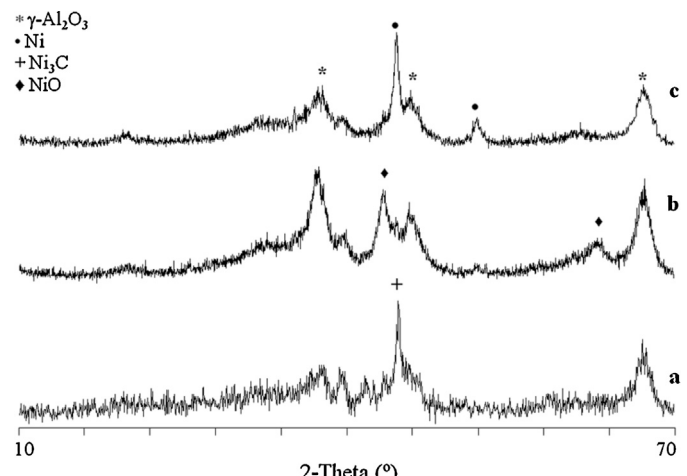


Fig. 11. XRD patterns of the Ni923 in the regeneration process, (a) after reaction, (b) after oxidation and (c) after reduction.

The catalyst regeneration by oxidation–reduction processes at 723 K was sufficient to regain full catalytic activity. The product distributions and glycerol conversion just before the deactivation process and after regeneration were similar in trend of conversion and selectivity, since the catalyst recovered the conversion of a highly active surface after regeneration. It is important to mention that during the oxidation process the Ni_3C carbide disappears forming a NiO phase which, after reduction, forms again the Ni phase (Fig. 11). The regeneration process was repeated for four cycles with the catalyst being fully reactivated in all cases. As already mentioned for the results in Table 4, when the spent Ni catalyst is activated by calcination without the reduction step, it results in low catalytic activity. Thus, the reduction step is crucial to activate the Ni sites.

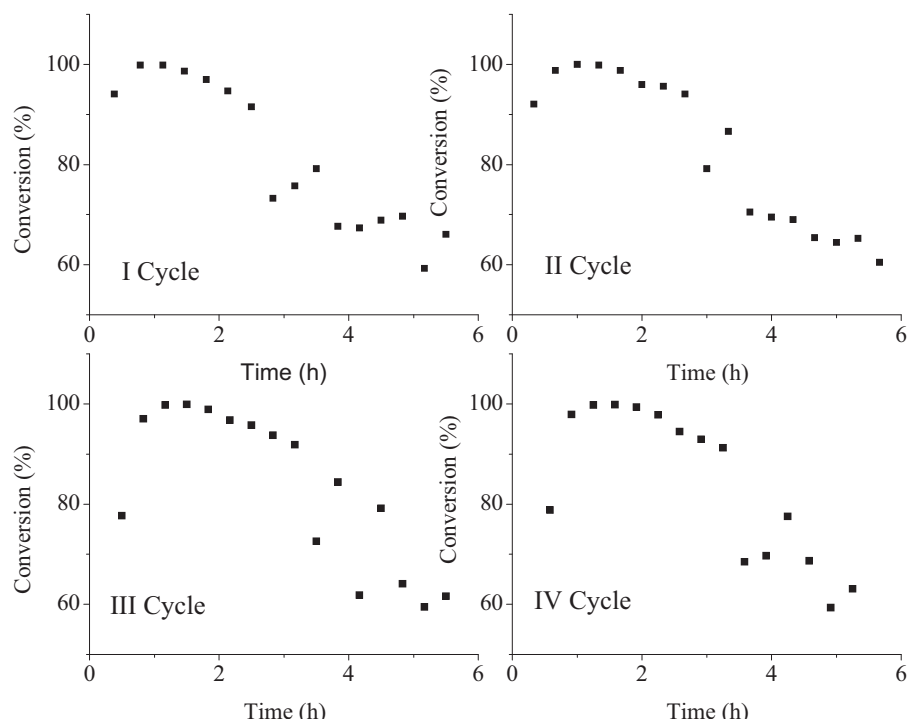


Fig. 10. Catalytic behavior in the conversion of glycerol of the Ni723 for different cycles of regeneration.

4. Conclusions

The catalytic conversion of glycerol was investigated on 10%Ni/γ-Al₂O₃ catalyst in gas phase. Different reduction treatments (between 623 and 1073 K) were applied to study their effects on the catalytic performance. The stability, selectivity and activity were modulated by the reduction conditions. Several routes of glycerol transformation such as dehydration, dehydrogenation and hydrogenolysis were observed giving different products (see Scheme 1). The bifunctional metal–acid property of the catalysts regulated the routes of the reactions and the stability of the catalysts. The main products obtained were hydroxyacetone, pyruvaldehyde, pyruvic acid, methyl lactate, lactide, acetaldehyde and methane. The source of deactivation was attributed to carbon deposition, Ni phase transformation giving NiO, and the formation of Ni₃C. The spent catalysts were totally regenerated after oxidation–reduction treatments. The oxidation step produces the transformation of Ni₃C into NiO. Furthermore, the reduction step is crucial to activate the Ni sites. Our findings indicated that the Ni particle size combined with the acidity modulated the catalytic performance of the Ni catalyst.

Acknowledgments

B.C. Miranda gratefully acknowledges the Universitat Rovira i Virgili (URV) and Universidad de Costa Rica for the financial support. We also would like to acknowledge European Synchrotron Radiation Facility (ESRF) and Brazilian National Laboratory Light Synchrotron (LNLS) for the user facilities for XRD and XANES measurements, respectively. Thanks for Ministry of Science and Technology for the financial support for the Juan de la Cierva program (JCI-2010-07328). We also would like to acknowledge Dr. Germán Castro, Dr. Iván da Silva and Dr. Alvaro Muñoz for the technical support offered at the ESRF (experiment MA1525). We also would like to acknowledge Dr. Joan Rosell, Dr. Luis Modesto Lopez and Edgar J. Güell for their help in the *in situ* XRD measurements. J.L. and F.M. are grateful to the ICREA Academia program.

References

- [1] J. Feng, H. Fu, J. Wang, R. Li, H. Chen, X. Li, *Catal. Commun.* 9 (2008) 1458–1464.
- [2] B.N. Zope, D.D. Hibbitts, M. Neurock, R.J. Davis, *Science* 330 (2010) 74–78.
- [3] A. Villa, G.M. Veith, L. Prati, *Angew. Chem. Int. Ed.* 49 (2010) 4499–4502.
- [4] S.H. Chai, H.P. Wang, Y. Liang, B.Q. Xu, *Green Chem.* 9 (2007) 1130.
- [5] M. Akiyama, S. Sato, R. Takahashi, K. Inui, M. Yokota, *Appl. Catal. A* 371 (2009) 60–66.
- [6] T.M. Che, US, 1987.
- [7] Y. Nakagawa, Y. Shimmi, S. Koso, K. Tomishige, *J. Catal.* 272 (2010) 191–194.
- [8] J. Chaminand, L. Djakovitch, P. Gallezot, P. Marion, C. Pinel, C. Rosier, *Green Chem.* 6 (2004) 359–361.
- [9] T. Miyazawa, Y. Kusunoki, K. Kunimori, K. Tomishige, *J. Catal.* 240 (2006) 213–221.
- [10] T. Miyazawa, S. Koso, K. Kunimori, K. Tomishige, *Appl. Catal. A* 329 (2007) 30–35.
- [11] M. Balaraju, V. Rekha, P.S.S. Prasad, B.L.A.P. Devi, R.B.N. Prasad, N. Lingaiah, *Appl. Catal. A* 354 (2009) 82–87.
- [12] L. Gong, Y. Lu, Y. Ding, R. Lin, J. Li, W. Dong, T. Wang, W. Chen, *Chin. J. Catal.* 30 (2009) 1189–1191.
- [13] L.B. Råberg, M.B. Jensen, U. Olsbye, C. Daniel, S. Haag, C. Mirodatos, A.O. Sjåstad, *J. Catal.* 249 (2007) 250–260.
- [14] M.A. Dasari, P.P. Kiatsimkul, W.R. Sutterlin, G.J. Suppes, *Appl. Catal. A* 281 (2005) 225–231.
- [15] S. Wang, H. Liu, *Catal. Lett.* 117 (2007) 62–67.
- [16] Z. Huang, F. Cui, H. Kang, J. Chen, X. Zhang, C. Xia, *Chem. Mater.* 20 (2008) 5090–5099.
- [17] C. Montassier, D. Giraud, J. Barbier, *Stud. Surf. Sci. Catal.* 41 (1988) 165–170.
- [18] A. Alhanash, E.F. Kozhevnikova, I.V. Kozhevnikov, *Catal. Lett.* 120 (2008) 307–311.
- [19] T. Kurosaka, H. Maruyama, I. Narabayashi, Y. Sasaki, *Catal. Commun.* 9 (2008) 1360–1363.
- [20] D. Roy, B. Subramiam, R.V. Chaudhari, *Catal. Today* 156 (2010) 31–37.
- [21] F. Vila, M. López Granados, M. Ojeda, J.L.G. Fierro, R. Mariscal, *Catal. Today* 187 (2012) 122–128.
- [22] E.S. Vasilidou, A.A. Lemonidou, *Appl. Catal. A* 396 (2011) 177–185.
- [23] W. Yu, J. Zhao, H. Ma, H. Miao, Q. Song, J. Xu, *Appl. Catal. A* 383 (2010) 73–78.
- [24] S. Xia, Z. Yuan, L. Wang, P. Chen, Z. Hou, *Appl. Catal. A* 403 (2011) 173–182.
- [25] L. Ma, D. He, Z. Li, *Catal. Commun.* 9 (2008) 2489–2495.
- [26] A. Perosa, P. Tundo, *Ind. Eng. Chem. Res.* 44 (2005) 8535–8537.
- [27] L. Jun-Cheng, X. Lan, X. Feng, W. Zhan-Wen, W. Fei, *Appl. Surf. Sci.* 253 (2006) 766–770.
- [28] C.V. Rode, R.B. Mane, A.S. Potdar, P.B. Patil, P.S. Niphadkar, P.N. Joshi, *Catal. Today* 190 (2012) 31–37.
- [29] Y. Nakagawa, K. Tomishige, *Catal. Sci. Technol.* 1 (2011) 179–190.
- [30] J. Wei, E. Iglesia, *J. Catal.* 224 (2004) 370–383.
- [31] R.B. Shalvoy, P.J. Reucroft, B.H. Davis, *J. Vac. Sci. Technol.* 17 (1980) 209.
- [32] I. Chen, D.W. Shiu, *Ind. Eng. Chem. Res.* 27 (1988) 429–434.
- [33] S.A. Stevenson, J.A. Dumesic, R.T. Baker, E. Ruckenstein, *Metal–Support Interactions in Catalysis, Sintering and Redispersion*, Van Nostrand Reinhold, New York, 1987.
- [34] Z. Paal, P.G. Menon, *Hydrogen Effects in Catalysis*, Marcel Dekker, Inc., New York, 1988.
- [35] J.R. Anderson, K.C. Pratt, *Introduction to Characterization and Testing of Catalysts*, Academic Press, New York, 1985.
- [36] I. Chen, S. Lin, D. Shiu, *Ind. Eng. Chem. Res.* 27 (1988) 926–929.
- [37] J.R.A. Sietsma, H. Friedrich, A. Broersma, M. Versluijs-Helder, A. Jos van Dillen, P.E. de Jongh, K.P.d. Jong, *J. Catal.* 260 (2008) 227–235.
- [38] G. Li, L. Hu, J.M. Hill, *Appl. Catal. A* 301 (2006) 16–24.
- [39] J.T. Richardson, M. Lei, B. Turk, K. Forster, M.V. Twigg, *Appl. Catal. A* 110 (1994) 217–237.
- [40] S. Velu, S.K. Gangwal, *Solid State Ionics* 177 (2006) 803–811.
- [41] W. Brockner, C. Ehrhardt, M. Gjikaj, *Thermochim. Acta* 456 (2007) 64–68.
- [42] S. Yuvaraj, L.F. Yuan, C.T. Huei, Y.C. Tih, *J. Phys. Chem. B* 107 (2003) 1044–1047.
- [43] K. Sing, D. Everet, R. Haul, L. Moscou, R. Pierotti, J. Rouquerol, T. Siemieniewska, *Pure Appl. Chem.* 57 (1985) 603–619.
- [44] J. Lif, I. Odenbrand, M. Skoglundh, *Appl. Catal. A* 317 (2007) 62–69.
- [45] C.H. Bartholomew, R.J. Farrauto, *J. Catal.* 45 (1976) 41–53.
- [46] W. Suprun, M. Lutecki, T. Haber, H. Papp, *J. Mol. Catal. A: Chem.* 309 (2009) 71–78.
- [47] A. Corma, P.J. Miguel, A.V. Orchilles, *J. Catal.* 145 (1994) 171–180.
- [48] F. Auneau, C. Michel, F. Delbecq, C. Pinel, P. Sautet, *Chem. Eur. J.* 17 (2011) 14288–14299.
- [49] M. Neuber, S. Ernst, H. Geerts, P.J. Grobet, P.A. Jacobs, G.T. Kokotailo, J. Weitkamp, *Stud. Surf. Sci. Catal.* 34 (1987) 567.
- [50] M.J.F.M. Verhaak, A.J. Van Dillen, J.W. Geus, *J. Catal.* 143 (1993) 187–200.
- [51] J. Guo, H. Lou, X. Zheng, *Carbon* 45 (2007) 1314.
- [52] J.R. Anderson, M. Boudart, *Catalysis: Science and Technology*, Springer-Verlag, Berlin, 1984.
- [53] C.H. Bartholomew, J.B. Butt, *Catalysts Deactivation*, Elsevier Science, Amsterdam, 1991.
- [54] D.A. Whan, C. Kemball, *Trans. Faraday Soc.* 64 (1968) 1102–1112.
- [55] P. Forzatti, L. Lietti, *Catal. Today* 52 (1999) 165–181.
- [56] C.H. Bartholomew, *Appl. Catal. A* 212 (2001) 17–60.
- [57] H. Atia, U. Armbruster, A. Martin, *J. Catal.* 258 (2008) 71–82.
- [58] Y.T. Chua, P.C. Stair, *J. Catal.* 213 (2003) 39–46.
- [59] L. Mendoza, R. Baddour-Hadjean, M. Cassir, J.P. Pereira-Ramos, *Appl. Surf. Sci.* 225 (2004) 356–361.
- [60] F.F. de Sousa, H.S.A. de Sousa, A.C. Oliveira, M.C. Junior, A.P. Ayala, E.B. Barros, B.C. Viana, J.M. Filho, A.C. Oliveira, *Int. J. Hydrogen Energy* 37 (2012) 3201–3212.
- [61] A.C. Ferrari, B. Kleinsorge, G. Adamopoulos, J. Robertson, W.I. Milne, V. Stoljan, L.M. Brown, A. LiBassi, B.K. Tanner, *J. Non-Cryst. Solids* 266–269 (2000) 765–768.
- [62] A.C. Ferrari, J. Robertson, *Phys. Rev. B* 61 (2000) 14095–14107.
- [63] F. Loviat, I. Czekaj, J. Wambach, A. Wokaun, *Surf. Sci.* 603 (2009) 2210–2217.
- [64] I. Czekaj, F. Loviat, F. Raimondi, J. Wambach, S. Biollaz, A. Wokaun, *Appl. Catal. A* 329 (2007) 68–78.
- [65] A. Bienholz, F. Schwab, P. Claus, *Green Chem.* 12 (2010) 290–295.